Anomalous transport in spin-half chains

Dissertation
zur
Erlangung des Doktorgrades (Dr. rer. nat.)
der
Mathematisch-Naturwissenschaftlichen Fakultät
der
Rheinischen Friedrich-Wilhelms-Universität Bonn

von
Ramsés J. Sánchez
aus
Caracas, Venezuela

Bonn, 12.06.2017

Dieser Forschungsbericht wurde als Dissertation von der
Mathematisch-Naturwissenschaftlichen Fakultät der Universität Bonn angenommen und ist auf dem Hochschulschriftenserver der ULB Bonn
http://hss.ulb.uni-bonn.de/diss_online elektronisch publiziert.

1. Gutachter:	Prof. Dr. Hartmut Monien
2. Gutachter:	apl. Prof. Dr. Ralf Bulla
Tag der Promotion:	17.10.2017
Erscheinungsjahr:	2018

Acknowledgements

Although many have been by my side during these last years one cannot but mention a few.

First of all I would like to thank Hartmut Monien, for is he who has taught me everything, and I mean everything, I know. His incredibly deep insights into math and physics problems apparently far apart, his funny anecdotes and witty remarks about almost everything, and his constant support have made my PhD studies a remarkable learning experience.

Second, I must thank Vipin Kerala Varma who has been like a second adviser to me. We have worked together throughout my PhD studies and cannot but hope we will keep collaborating, for I have learned a lot with him. Likewise I also thank Vadim Oganesyan with whom I just started collaborating and who has shown so much support towards my ideas.

Third, I thank Andreas Wißkirchen, Patricia Zündorf and Petra Weiß who were always willing to help in every situation. I also thank Ralf Bulla who agreed to be my (official) second advisor and who has also always been willing to help.

Last but not least I have to thank my friends César and César, Giulia and Rocio. They have endure the darkest of times with me, and gave me the strength to keep going.

Thanks to you all.

Contents

CHAPTER 1

Introduction

At high temperatures any local deviation from thermal equilibrium in a generic many-body system has a large number of channels available into which it can decay. In such an scenario most excited degrees of freedom relax exponentially fast, within times determined by the microscopic interactions, i.e. times which are small on a macroscopic scale. However, if the degree of freedom in question is conserved, that is, a constant of motion, the corresponding initial imbalance can only relax by spreading slowly ("diffusing") over the entire system as a long-lived collective mode.

To be precise, let us consider the (average) longitudinal magnetization density $M(\boldsymbol{r}, t)$ at the space-time point $(\boldsymbol{r}, t)$ in a magnetic system invariant under rotations about the $\hat{z}$-axis. The U(1) symmetry implies the total magnetization along the longitudinal axis is conserved, that is

$$\frac{d}{dt}\left\{\int d^3r\, M(\boldsymbol{r}, t)\right\} = 0. \tag{1.1}$$

Note the conservation law (1.1) also has a differential form, the continuity equation

$$\frac{\partial M(\boldsymbol{r}, t)}{\partial t} + \boldsymbol{\nabla} \cdot \boldsymbol{j}_s(\boldsymbol{r}, t) = 0, \tag{1.2}$$

where the spin current $\boldsymbol{j}_s(\boldsymbol{r}, t)$, as the magnetization, is an average *l*ocal density.

Suppose $M(\boldsymbol{r}, t)$ deviates from its equilibrium value. The continuity equation (1.2) alone does not completely determine how this initial inhomogeneous density becomes uniform, it only restricts the relaxation process a little. To solve for $M(\boldsymbol{r}, t)$ we therefore need a second equation relating the spin current to the magnetization density. Now, at high temperatures one may think the magnetic system as being a spin fluid featuring two kinds of relaxation processes: first, within a short *correlation time* τ_0, thermal equilibrium is approximately established in small regions of macroscopic size,[1] with a local magnetization density as a macroscopic state variable; second, the resulting magnetization gradient at longer length scales causes a much slower net flow of magnetization, so as to attain uniformity in coordinate space. The latter is a hydrodynamic process characterized by a *relaxation time* τ_r which is much longer than the

[1] Regions which are small as compared to the size of the entire system, and yet big enough to include a large fraction of magnetic moments.

microscopic relaxation time τ_0. Thus, in the hydrodynamic limit, for time intervals $\tau_r > t \gg \tau_0$ during which all properties of the system vary very slowly in space and time, one may write

$$\boldsymbol{j}_s(\boldsymbol{r}, t) = -D_s \, \boldsymbol{\nabla} M(\boldsymbol{r}, t), \tag{1.3}$$

where $D_s > 0$ is the spin diffusion coefficient. The phenomenological relation (1.3), first proposed in [1] for spins on nuclei fixed on a lattice, entails the current follows changes in the magnetization *instantaneously*, that is, it implies the rate of dissipation is Markovian (a memoryless process).

Inserting eq. (1.3) into (1.2) yields the diffusion equation for the magnetization

$$\frac{\partial M(\boldsymbol{r}, t)}{\partial t} = D_s \, \nabla^2 M(\boldsymbol{r}, t), \tag{1.4}$$

which is solved in the thermodynamic limit by Fourier (Laplace) transforming the spatial (temporal) coordinate to find

$$\tilde{M}(\boldsymbol{k}, z) = \frac{i}{z + i D_s \, k^2} \, M(\boldsymbol{k}, 0), \tag{1.5}$$

with $\mathrm{Im}\, z > 0$ and $\boldsymbol{k}$ the wave vector of the magnetic fluctuations. Note from eq. (1.5) the diffusion process is reflected in a pole on the negative imaginary axis at $z = -iD_s \, k^2$. Using Cauchy's residue theorem we can calculate the inverse Laplace transform of eq. (1.5) to be

$$M(\boldsymbol{k}, t) = e^{-D_s k^2 t} \, M(\boldsymbol{k}, 0), \tag{1.6}$$

which displays the characteristic properties of a *hydrodynamic mode* [2, 3] — a spatially sinusoidal collective fluctuation which for long wavelengths $\lambda = 2\pi \, |\boldsymbol{k}|^{-1}$ is exponentially damped, with a lifetime $\tau_r = (D_s k^2)^{-1}$ which diverges as $|\boldsymbol{k}|$ approaches zero. In other words, a local deviation of the conserved magnetization density from its equilibrium value cannot disappear locally (which could happen rapidly) but can only relax by diffusing over the entire system as a collective mode.

Finally, assuming $M(\boldsymbol{r}, 0) = M \, \delta(\boldsymbol{r})$ one can write down the inverse Fourier transform of eq. (1.6) as

$$M(\boldsymbol{r}, t) = \frac{M}{(4\pi D_s)^{3/2}} \, t^{-3/2} \, e^{-r^2/(4tD_s)}. \tag{1.7}$$

Eq. (1.7) says the phenomenological relation (1.3) — valid in the long-time regime $t \gg \tau_0$ only — entails the spin modes in the system behave as independent Gaussian fluctuations. The slow relaxation of $M(\boldsymbol{r}, t)$ can then be interpreted as a random walk of the magnetization through a cubic lattice, just as in classical diffusion. A local distortion of the longitudinal magnetization density thus has a characteristic size which scales as a power law of time in the hydrodynamic limit

$$\langle \, (\Delta x)^2 \, \rangle \sim t^d, \tag{1.8}$$

for generic d-dimensional systems, provided a relaxation time τ_0 small on macroscopic scales

exists.

In this thesis we shall study high-temperature spin transport in anisotropic spin-1/2 chains for which the total magnetization along the $\hat{z}$-axis is conserved. However, these chains will show fundamentally different relaxation properties from the generic phenomenological Markovian-diffusive picture drawn above. Indeed, among the many reasons that make one-dimensional systems special, and their finite-temperature transport properties radically different from systems in higher dimensions — even at *infinite temperatures* — is that, due to momentum and energy conservation, the scattering of two identical particles can only rearrange their incoming momenta, which implies the corresponding scattering amplitude cannot but be a phase shift. Hence two-body collisions alone cannot thermalize a one-dimension fluid of identical particles [4]. What is truly remarkable is that in certain class of one-dimensional models, many-body scattering processes are *exactly equivalent* to a sequence of two-body collisions.[2]

Models belonging to this class of nonergodic dynamical systems are known as *quantum integrable models* and feature stable collective excitations which undergo completely ellastic scattering. The underlying dynamical constrains result in a macroscopic number of *local* (and *quasilocal*) conserved quantities [6–9] which can prevent generic correlation functions from fully decaying. This renders the timescale-separation assumption of the phenomenological diffusion theory inapplicable. Transport properties in integrable models are therefore expected to be anomalous, characterized by the coexistence of both ballistic and diffusive transport channels. More generally, one may think local fluctuations of conserved densities in integrable systems scale anomalously in the hydrodynamic limit as

$$\langle\, (\Delta x)^2 \,\rangle \sim t^{\,1-\alpha}, \quad \text{with } |\alpha| \leq 1. \tag{1.9}$$

In contrast, the more common diffractive models, that is, models featuring nonelastic scattering, are said to be *nonintegrable*. These exhibit chaotic spectra and are effectively described by random matrix theory [10]. Furthermore, due to the statistical properties of their highly excited eigenstates, finite-temperature correlation functions in these models usually decay very rapidly. In this case the phenomenological diffusion theory is expected to provide a good description of the long-time finite-temperature dynamical behavior.

Remarkably, newly synthetized families of quasi one-dimensional materials characterized by weak interchain coupling and low disorder — and described by quantum integrable models — have been found to display unconventional (nondiffusive) transport properties. In the spin-chain context, for example, a major breakthrough was the identification of Sr_2CuO_3 crystals as nearly ideal realizations of the one-dimensional (integrable) spin-1/2 antiferromagnetic Heisenberg model [11]. Two observations are noteworthy: first, the spin-mediated heat conductivity in this compound was found to be strongly anisotropic and very large in magnitude along the chain direction at high temperatures, exceeding the phonon contribution quite substantially [12, 13]. Interestingly enough, the energy current in the corresponding Heisenberg model is conserved, which entails heat transport is trivially ballistic [9]. The anomalously large value of the heat conductivity in Sr_2CuO_3 is thus usually considered a reflection of dissipationless energy

[2] This property is the very essence behind *the Bethe Ansatz* — a many-body wave function entirely composed of elements from two-particle wave functions, originally proposed by Hans Bethe to find the exact eigenvalues and eigenfunctions of the spin-1/2 one-dimensional Heisenberg model [5].

transport within the pure chain. Second, nuclear magnetic resonance spectroscopy (NMR) experiments revealed the low-frequency long-wavelength finite-temperature spin dynamics in Sr_2CuO_3 is diffusive, but with a fairly large diffusion constant [14, 15]. Although the issue of finite-temperature spin transport in the Heisenberg chain is long standing and controversial, the large diffusion constant observed in Sr_2CuO_3 is also commonly attributed to the integrability of the chain.

Now, in systems as Sr_2CuO_3 additional interactions not included in their corresponding integrable models are always present. The nontrivial conservation laws of the latter are thus violated by perturbations, which can often be considered to be small. How are the transport properties of integrable models modified by weak "integrability-breaking" perturbations? — one may ask. A possible answer to this question is that, if the perturbation is small enough, the "nearly conserved" quantities in the (nonintegrable) system govern its long-time dynamical properties [16, 17]. This picture however does not always hold, as we explicitly show in chapter 4.

In this work we investigate spin transport properties in both integrable and nonintegrable spin chains at zero and infinite temperatures, and question in the latter limit whether diffusion is always normal (Markovian) when the spin current decays rapidly. Specifically, we study spin transport in the integrable XXZ Heisenberg model — defined in section 1.2 — and its response to integrability-breaking next nearest-neighbor spin flips. Let us now briefly outline our main results.

We start in chapter 2 by investigating the consequences of breaking integrability on the zero-temperature transport properties of the model using exact diagonalization [18]. There we note that depending on the sign of the spin-flip perturbation the model can display in-plane frustration and localize the spin degrees of freedom. We find an interaction-induced enhancement of transport when the model is frustrated. The enhancement occurs because the spin anisotropy, which favors Néel-like configurations, effectively reduces the frustration in the system thereby increasing the strength of the spin stiffness. The latter is defined in section 1.1. Surprisingly, a similar phenomenon is observed at infinite temperature later in this work, with much richer dynamical properties.

The rest of the thesis focuses on both DC and AC response in the infinite temperature limit.

In chapter 3 we consider the issue of ballistic transport in the integrable chain. There we revisit the numerical problem of computing the high-temperature spin stiffness using exact diagonalization, to explain some finite-size extrapolation inconsistencies found in the literature. Within the canonical ensemble and for states with zero total magnetization, we find the stiffness vanishes exactly due to spin-inversion symmetry for all but the fractal set of anisotropies $\tilde{\Delta}_{MN} = \cos(\pi M/N)$, with $N \in \mathbb{N}^+$, $M < N$ coprimes. This holds provided system sizes $L \geq 2N$, for which states with different spin-inversion signature become degenerate, due to the underlying sl_2 quantum loop symmetry. We thus confirm spin transport is ballistic within the gapless phase of the XXZ chain and find the current-carrying sl_2-loop degenerate states to play an important role in contributing to the thermodynamic limit of the spin stiffness. At the isotropic point and within the gapped phase, in contrast, the spin stiffness is found to vanish in the thermodynamic limit, independent of symmetry or ensemble. Our analysis further demonstrates how convergence to the thermodynamic limit within the gapless phase may be accelerated and the previously reported finite-size anomalies overcome: the spin stiffness extrapolates

nicely in the thermodynamic limit to either the recently computed exact lower-bound or the Thermodynamic Bethe Ansatz result provided both spin-inversion and sl_2-loop symmetry are broken *or* the system size $L \geq 2N$.

In chapter 4 we investigate instead high-temperature AC response, both in the integrable and nonintegrable limits of our model. Our analysis is based on (i) a three-parameter Ansatz for the memory function whose long-wavelength limit describes the Kubo conductivity, which we introduce in section 1.1, and (ii) an exact-diagonalization evaluation of the regular component of the Kubo formula for small spin chains. The Ansatz is chosen as to capture the possibility of anomalous diffusion at and close to the integrable limit, and yields an expression for the low-frequency power-law exponent of the regular conductivity in terms of the microscopic parameters of the model. Our main results can be summarized as follows: in the integrable XXZ model we find (i) the regular component of the conductivity to show subleading subballistic low-frequency power law behavior within the gapless phase; (ii) the isotropic point to be superdiffusive, with a frequency dependent conductivity $\sigma(\omega \to 0) \sim |\omega|^{-3/7}$ in close numerical agreement with t-DMRG results[19–21]; and (iii) a diffusion constant linearly proportional to the weak nearest-neighbor spin-flip amplitude deep into the gapped phase. After breaking integrability we find that (iv) while positive NNN spin flips enhance spin transport, there is a narrow interval of negative NNN spin-flip amplitudes for which transport is strongly suppressed; and that (v) if the perturbing NNN spin-flips amplitudes are small (i.e. close to the integrable limit) the model displays anomalous diffusion on intermediate time scales. This behavior is predicted by the Ansatz and corroborated by the exact-diagonalization computations. Thus we present a semi-heuristic approach applicable to integrable and nonintegrable systems alike, capable of describing both qualitative and quantitative aspects of quantum transport. We note that similar anomalous transport properties at low frequencies in *thermal* transport have also been observed in perturbed Heisenberg chains with NNN couplings [17]. The anomalies were there shown to be inherited from the integrable point and associated with near-conserved quantities. However, in that study the thermal anomaly showed up as a J_2^{-4} effect, independent of the sign of J_2.

The main quantity we focus on is the spin Kubo conductivity, which within linear response theory is defined as the ratio between the spin current density $\langle\, \hat{j} \,\rangle_{\text{non-eq}}$ and the gradient of an external magnetic field $h(k, \omega)$

$$\langle\, \hat{j}(k, \omega) \,\rangle_{\text{non-eq}} = \sigma(k, \omega)\, ik\, h(k, \omega). \tag{1.10}$$

In what follows we make sense of eq. (1.10) and introduce the concepts that will be used throughout this work.

1.1 Linear dynamical response and Kubo conductivity

The dynamical properties of the spin chains we consider are disclosed by stimulating the system with external disturbances — such as neutron beams and magnetic fields — and investigating how it responds. This (out of equilibrium) dynamical response can be expressed in terms of time-dependent thermodynamic expectation values of spin operators in the equilibrium state as

we now show.

Assume our spin chains are described by some model Hamiltonian H. In the presence of an external magnetic field the Hamiltonian becomes explicitly time dependent

$$H'(t) = H + \delta H(t) = H - \sum_{l}^{L} \hat{S}_l^z \, h(l,t), \tag{1.11}$$

where S_l^z is the $\hat{z}$-component of the spin-1/2 operator at site l of a L-site periodic chain, and $h(l,t)$ is the local time-dependent magnetic field coupling the spin. A gradient of the magnetic field along the chain produces a magnetization imbalance which in turn generates a spin current density. The latter is described by $\langle\, \hat{j}_l(t) \,\rangle_{\text{non-eq}}$ — the thermodynamic expectation value of the (yet undefined) current operator in the *nonequilibrium state*. Following [3] we define such an expectation value as

$$\langle\, \hat{j}_l(t) \,\rangle_{\text{non-eq}} = \text{Tr}\left\{\hat{\rho}(t)\, \hat{j}_l\right\}, \tag{1.12}$$

where the density matrix $\hat{\rho}(t)$ encoding the nonequilibrium dynamics is, *to first order* in $\delta H(t)$

$$\hat{\rho}(t) = \hat{\rho}_0 + \delta\hat{\rho}(t), \tag{1.13}$$

with $\hat{\rho}_0 \equiv \hat{\rho}(-\infty)$ the density matrix describing the (equilibrium) state of the system in the remote pass, when the perturbation δH is absent, and

$$\delta\hat{\rho}(t) = \frac{1}{i\hbar} \int_{-\infty}^{t} d\tau e^{-iH(t-\tau)/\hbar} \, [\delta H(\tau), \hat{\rho}_0] \, e^{iH(t-\tau)/\hbar}. \tag{1.14}$$

Here we choose the canonical ensemble $\hat{\rho}_0 = e^{-\beta H}/Z$, with $Z = \text{Tr} e^{-\beta H}$ the partition function and β the inverse temperature. The derivation of eq. (1.14) is standard and can be found in e.g. [3]. The linear spin current response to $\delta H(t)$ then follows from the last three equations above

$$\begin{aligned} \langle\, \hat{j}_l(t) \,\rangle_{\text{non-eq}} &= \text{Tr}\left\{ -\frac{1}{i\hbar} \sum_{m}^{L} \int_{-\infty}^{t} d\tau \, e^{-iH(t-\tau)} [\hat{S}_m^z, \, \hat{\rho}_0] \, e^{iH(t-\tau)/\hbar} \, \hat{j}_l \, h(m,\tau) \right\} \\ &= \frac{i}{\hbar} \int_{-\infty}^{t} d\tau \sum_{m}^{L} \text{Tr}\left\{ [\hat{j}_l(t), \hat{S}_m^z(\tau)] \, \hat{\rho}_0 \right\} h(m,\tau), \end{aligned} \tag{1.15}$$

where we use $\text{Tr}\{\hat{j}\,\hat{\rho}_0\} = 0$ since there is no current in the equilibrium state.

Given that the models we consider are translationally invariant in both time and space we can Fourier transform eq. (1.15) and write

$$\langle\, \hat{j}(k,\omega) \,\rangle_{\text{non-eq}} = \Lambda(k,\omega)\, h(k,\omega), \tag{1.16}$$

where we introduced the complex response function

$$\Lambda(k,\omega) = \frac{i}{\hbar L}\int_0^\infty dt e^{i(\omega+i\delta)t}\langle\,[\hat{j}(k,t),\hat{S}^z(-k,0)]\,\rangle, \tag{1.17}$$

with $\langle\,\cdot\,\rangle \equiv \mathrm{Tr}\{\,\cdot\,\rho_0\}$ the equilibrium expectation value, and δ a positive infinitesimal real number. Now, using the continuity equation

$$\partial_t \hat{S}\,(k,t) = -ik\,\hat{j}(k,t), \tag{1.18}$$

we can partially integrate eq. (1.17) to find

$$\Lambda(k,\omega) = \frac{1}{\hbar L(\omega+i\delta)}\left\{-\langle\,[\hat{j}(k,0),\hat{S}^z(-k,0)]\,\rangle + ik\int_0^\infty dt e^{i(\omega+i\delta)t}\langle\,[\hat{j}(k,t),\hat{j}(-k,0)]\,\rangle\right\}. \tag{1.19}$$

The second term on the right hand side of (1.19) — which we label $(ik)\,I(k,\omega)$, has the spectral representation

$$I(k,\omega) = i\int_{-\infty}^\infty dx \sum_{n,m}\frac{e^{-\beta E_n}}{Z}\langle\,n\,|\,\hat{j}(k)\,|\,m\,\rangle\langle\,m\,|\,\hat{j}(-k)\,|\,n\,\rangle\frac{1-e^{-\beta(E_m-E_n)}}{\omega+i\delta-x}\delta(x-E_m+E_n), \tag{1.20}$$

where both summations run over the eigenstates $H\,|n\rangle = E_n\,|n\rangle$. We now define the complex longitudinal conductivity as

$$\sigma(k,\omega) \equiv \lim_{\delta\to 0}\frac{\Lambda(k,\omega)}{ik}, \tag{1.21}$$

so that the relation

$$\langle\,\hat{j}(k,\omega)\,\rangle_{\text{non-eq}} = \sigma(k,\omega)\,ik\,h(k,\omega), \tag{1.22}$$

yields the Kubo formula for the spin conductivity in the long-wavelength limit [22]

$$\sigma'(\omega) = D\,\delta(\omega) + \sigma^{\text{reg}}(\omega). \tag{1.23}$$

The weight "D" of the Dirac δ-function is known as *spin stiffness* (or spin Drude weight) and quantifies the nondecaying components of the spin current operator, whereas $\sigma^{\text{reg}}(\omega)$ defines the regular contribution of the spin conductivity. These quantities are defined as

$$\begin{aligned} D &\equiv \pi\lim_{\omega\to 0}\omega\,\mathrm{Im}\left\{\lim_{k\to 0}\sigma(k,\omega)\right\} \\ &= -\frac{\pi}{L}\langle\,\hat{T}\,\rangle - \frac{2\pi}{L}\sum_{\substack{n,m\\ E_n\neq E_m}}\frac{e^{-\beta E_n}}{Z}\frac{|\langle\,m\,|\,\hat{j}\,|\,n\,\rangle|^2}{E_m-E_n}, \end{aligned} \tag{1.24}$$

where we introduced the kinetic energy operator $\hat{T} = \lim_{k\to 0}[\hat{S}^z(-k),\hat{j}(k)]/k$ and

$$\begin{aligned}\sigma^{\text{reg}}(\omega) &\equiv \text{Re}\left\{\lim_{k\to 0}\sigma(k,\omega)\right\} \\ &= \frac{\pi}{L}\frac{1-e^{-\beta\omega}}{\omega}\sum_{\substack{n,m \\ E_n\neq E_m}}\frac{e^{-\beta E_n}}{Z}|\langle\, m\,|\,\hat{j}\,|\,n\,\rangle|^2\delta(\omega-E_m+E_n).\end{aligned} \tag{1.25}$$

Clearly a finite spin stiffness gives an infinite conductivity and signals *ballistic* transport. On the other hand, the zero-frequency limit of the regular conductivity yields the DC conductivity

$$\sigma_{DC} \equiv \lim_{\omega\to 0}\sigma^{\text{reg}}(\omega). \tag{1.26}$$

From our discussion above it should be clear that models described by the phenomenological spin diffusion theory — as one assumes is the case for generic nonintegrable models — must have a vanishing spin stiffness and a finite σ_{DC}. The spin stiffness and the regular conductivity are the quantities we analyze by means of exact diagonalization and a set of exact sum-rule moment relations. Let us now define the model we shall investigate throughout this thesis.

1.2 The model

We consider a spin-chain of length L with periodic boundary conditions described by the Hamiltonian

$$H = \frac{J_1}{2}\sum_j^L(\hat{S}^+_j\hat{S}^-_{j+1}+\hat{S}^+_{j+1}\hat{S}^-_j)+\frac{J_2}{2}\sum_j^L(\hat{S}^+_j\hat{S}^-_{j+2}+\hat{S}^+_{j+2}\hat{S}^-_j)+\Delta\sum_j^L\hat{S}^z_j\hat{S}^z_{j+1}, \tag{1.27}$$

where the raising and lowering spin operators $(\hat{S}^+_j\hat{S}^-_{j+i}+\text{h.c})$ flip pairs of spins at sites j and $j+i$ with amplitude J_i and the spin anisotropy $\Delta > 0$ controls the strength of the spin-spin antiferromagnetic interaction. Note that although the sign of J_1 have no effect on the physics of the model, that of J_2 does have a nontrivial effect. Indeed, if J_2 is negative nearest- and next-nearest neighbor flips are energetically favorable, whereas if J_2 is positive the corresponding energy cannot be simultaneously minimized. Thus we say the model shows in-plane frustration when $J_2 > 0$. We will see the sign of J_2 strongly affects the dynamical properties of the model, both at zero and at infinite temperatures. Finally, when $J_2 = 0$ the model reduces to the well known integrable XXZ Heisenberg model.

In what follows we set J_1 as our energy scale.

1.2.1 Global symmetries

The Hamiltonian (1.27) is invariant under spin rotations about the z-axis $\hat{m}_z$, lattice translations $\hat{K}$, parity $\hat{P}$ and spin-inversion $\hat{Z}$[3]

[3] Not to be confused with the partition function Z.

The parity operator, with eigenvalues $p = \pm 1$, is defined as

$$\hat{P}\hat{S}^{\gamma}_{j}\hat{P} = \hat{S}^{\gamma}_{L-j}, \quad \text{with } \gamma = \pm, z. \tag{1.28}$$

Likewise the spin-inversion operator, with eigenvalues $z = \pm 1$, is defined such as

$$\hat{Z}\hat{S}^{\pm}_{j}\hat{Z} = \hat{S}^{\mp}_{j}, \quad \hat{Z}\hat{S}^{z}_{j}\hat{Z} = -\hat{S}^{z}_{j}. \tag{1.29}$$

Therefore, in addition to the total energy, the total magnetization along the z-axis "m_z", the total crystal momentum "K", parity "p" and z-parity "z" are global conserved quantities of the system, and this holds for all values of $J_{(1,2)}$ and $\Delta \in \mathbb{R}$. This set of symmetries will be used in chapters 3 and 4 to block-diagonalize a matrix representation of eq. (1.27).

1.2.2 Spin current operator

The (transversal) component of the total spin conductivity operator along the spin chain is defined as

$$\hat{j} = \sum_{l}^{L} \hat{j}_l. \tag{1.30}$$

Since the total magnetization m_z is conserved, the local current operator $\hat{j}_l$ satisfies the continuity equation

$$\hat{j}_l - \hat{j}_{l-1} = -i[H, \hat{S}^{z}_{l}], \tag{1.31}$$

which gives

$$\hat{j} \;=\; i\frac{J_1}{2}\sum_{j}^{L}\left(\hat{S}^{+}_{j+1}\hat{S}^{-}_{j} - \hat{S}^{+}_{j}\hat{S}^{-}_{j+1}\right) + iJ_2\sum_{j}^{L}\left(\hat{S}^{+}_{j+2}\hat{S}^{-}_{j} - \hat{S}^{+}_{j}\hat{S}^{-}_{j+2}\right) \tag{1.32}$$

Note this operator is odd under both parity and spin-inversion, i.e.

$$\hat{O}\,\hat{j}^{z}\,\hat{O} = -\hat{j}^{z}, \quad \text{for } \hat{O} = \hat{P}, \hat{Z} \tag{1.33}$$

1.2.3 At high temperatures, when is transport ballistic?

The model (1.27) is integrable when $J_2 = 0$ and nonintegrable otherwise. The spin stiffness in nonintegrable models is expected to vanish in the thermodynamic limit, and indeed numeric simulations support this expectation [23]. In contrast, integrable models have a macroscopic number of local conserved quantities $\hat{Q}_m$ which may have a finite overlap with the spin current operator, thereby preventing current-current correlations from completely decaying. In the XXZ model all these local conserved quantities are even under spin-inversion [9], whereas $\hat{j}$ is odd, and consequently the thermodynamic expectation value $\langle \hat{j}\,\hat{Q}_m \rangle$ vanishes identically. However, if spin inversion symmetry is broken by e.g. an external magnetic field, a finite magnetization

density or a magnetic flux — the latter only for finite spin rings, the expectation value $\langle \hat{j}\, \hat{Q}_m \rangle$ need no vanish. In fact, using an inequality due to Mazur [24] it has been shown that at high temperature and for finite magnetization densities, the spin stiffness in the XXZ model has the finite lower bound

$$D \geq \frac{\beta}{2} \frac{8\,\Delta^2\, m_z^2\,(1/4 - m_z^2)}{1 + 8\,\Delta^2 (1/4 + m_z^2)}, \tag{1.34}$$

where β is the inverse temperature [9] . Eq. (1.34) accounts for the overlap of $\hat{j}$ with the conserved local energy current, and entails the XXZ mode displays ballistic transport for finite m_z and $\Delta \in \mathbb{R}$.

At exactly zero magnetization eq. (1.34) is inconclusive, and one needs to distinguish between three regimes with different transport properties. When $\Delta < 1$ there exists a one-parameter family of quasilocal exact conserved quantities, which includes operators of odd q-parity having a finite overlap with $\hat{j}$. This family of quasilocal operators, together with Mazur's inequality, yields a finite lower bound for the spin stiffness and entails ballistic transport within the gapless phase ($\Delta < 1$) [25, 26]. In chapter 3 we shall look in detail into this regime. At $\Delta = 1$ the global SU(2) symmetry of the model can be used to construct a rigorous upper bound for the spin stiffness. This upper bound vanishes with the magnetization, thus implying the absence of ballistic transport at the isotropic point ($\Delta = 1$) [27, 28]. Finally, within the gapped phase ($\Delta > 1$) no rigorous results are known but numerical simulations point towards a vanishing spin stiffness [23, 29], as can be seen e.g. in Fig. 3.2. Summarizing, spin transport in the integrable XXZ model, that is eq.(1.27) with $J_2 = 0$, for anisotropies $\Delta \geq 1$ and zero magnetization densities is *nonballistic*, i.e. it is dominated by the regular part of the Kubo conductivity (1.25).

CHAPTER 2

Interaction-induced transport enhancement in frustrated spin chains

This chapter is special in the sense that, as opposite to the other chapters in this work, it deals with transport properties of our model (1.27) at precisely *zero temperature*. Our aim is to make a simple observation regarding the sign of the spin-flip amplitude J_2 and its effect on the zero-temperature spin stiffness [18]. Indeed, as pointed out before the presence of a *positive* J_2 yields *in-plane* frustration: if $J_2 > 0$ the energy associated with nearest and next-nearest neighbor spin flips cannot be simultaneously minimized, whereas if $J_2 < 0$ both processes lower the ground-state energy. At zero temperature J_1 and *negative* J_2 simply increase the ability of the system to sustain dissipationless spin transport. In contrast, when the model is frustrated dimer spin configurations are preferred instead, as can be seen by e.g. considering the point in parameter space where $J_2 = J_1/2$ and $\Delta = 0$ which has the two products of dimer states

$$\prod_{j \in \text{even or odd}} |\uparrow_j\downarrow_{j+1} + \downarrow_j\uparrow_{j+1}\rangle, \tag{2.1}$$

as exact ground states [30]. The spin anisotropy competes with this kind of order by favoring Néel-like configurations wherein neighboring spins align antiparallel to each other. The model thus displays three quantum phases, namely a gapless spin liquid, a gapped dimerized phase and a gapped Néel phase, the critical properties of which have been extensively investigated in [30, 31]. We will work along a contour of the phase diagram presented by Mishra et al. [30] and numerically show the competition between dimerized and Néel order results in an interaction-induced enhancement of the spin stiffness within the gapless spin liquid phase of the model. Surprisingly, we will find a similar phenomenon in the finite-frequency response of the model *at infinite temperatures* in chapter 4,

2.1 Drude weight, persistent currents and superfluid density

We start by pointing out there is an alternative way of interpreting the spin stiffness that proves very convenient for the numeric computation of D and provides a natural route to introduce the concept of *persistent currents* in mesoscopic systems. Instead of a magnet, the quantum system described by our model (1.27) can be viewed as a lattice gas of hard-core bosons with nearest-neighbor repulsive interactions in a L-site ring. In such a representation an up (down) spin at site j corresponds to a particle (hole) at that same site, created by the operator $\hat{S}_j^+$ ($\hat{S}_j^-$), while the boson number operator is essentially given by $\hat{S}_j^z$. With this picture in mind we shall refer to the spin stiffness as Drude weight throughout this chapter. Likewise we shall identify the spin liquid, dimer and Néel phases with superfluid, bond-ordered and charge density wave phases, respectively. Now suppose the particles of the gas are charged and the ring is threaded by a magnetic flux Φ. The flux gives rise to a static vector potential $A = \Phi/L$ along the path of the particles, which can be gauged away into a Peierls phase factor [32]

$$\hat{S}_j^{\pm} \to \exp\left\{\pm i\frac{\Phi}{L}j\right\}\hat{S}_j^{\pm}, \tag{2.2}$$

and hence enters as a parameter of the Hamiltonian.

The presence of the flux perturbs the energy levels of the quantum mechanical system and produces a persistent thermodynamic flow $J \propto -dF/d\Phi$ around the ring, where F stands for the free energy of the system. Indeed, although F refers to a thermal equilibrium state with Φ fixed, it remains meaningful if Φ varies adiabatically. The resulting rate of change of the free energy represents the work per unit time delivered to the system. Under the application of the external voltage $V \propto -d\Phi/dt$ and with a total current J circulating around the ring one thus has, roughly

$$\frac{dF}{dt} = \frac{dF}{d\Phi}\frac{d\Phi}{dt} = JV, \tag{2.3}$$

from which it follows $J = -dF/d\Phi$ [33, 34]. A notable example of this effect occurs in low temperature mesoscopic rings in the presence of a static magnetic field, wherein the electronic wave function can retain the *Aharonov-Bohm phase* acquired throughout the ring [35] and coherently extend over the whole system, thereby generating a persistent current [36]. Note this is also true for non-superconducting materials, as has been observed on copper [37] and gold [38] rings[1].

Expanding the flux-dependent Hamiltonian up to second order in Φ we find

[1] Nevertheless, the persistent currents found in those experiments are orders of magnitude smaller than those in superconductors [34]

$$H[\Phi] = H[0] + \left\{ \sum_j^L i \frac{J_1}{2} \left(\hat{S}^+_{j+1} \hat{S}^-_j - \hat{S}^+_j \hat{S}^-_{j+1} \right) + i J_2 \left(\hat{S}^+_{j+2} \hat{S}^-_j - \hat{S}^+_j \hat{S}^-_{j+2} \right) \right\} \frac{\Phi}{L} + \left\{ \sum_j^L \frac{J_1}{2} \left(\hat{S}^+_{j+1} \hat{S}^-_j + \hat{S}^+_j \hat{S}^-_{j+1} \right) + 2 J_2 \left(\hat{S}^+_{j+2} \hat{S}^-_j + \hat{S}^+_j \hat{S}^-_{j+2} \right) \right\} \frac{\Phi^2}{L^2} + O[\Phi^3], \quad (2.4)$$

where $H[0]$ labels the unperturbed (unfluxed) Hamiltonian. The term linear in Φ in eq. (2.4) is nothing but the *paramagnetic* current, as obtained from the continuity equation in eq. (1.32). The term quadratic in Φ is the diamagnetic current and corresponds to the kinetic energy operator $\hat{T}$. Note this operator also shows up in eq. (1.24).

The ground state $|\, 0[\Phi] \,\rangle$ of the perturbed Hamiltonian $H + \hat{j}\,(\Phi/L)$ can be written in terms of the unperturbed eigenstates by using standard perturbation theory

$$|\, 0[\Phi] \,\rangle = |\, 0 \,\rangle - \frac{\Phi}{L} \sum_{m \neq 0} |\, m \,\rangle \frac{\langle\, m \,|\, \hat{j} \,|\, 0 \,\rangle}{E_m - E_0} + O\,[\Phi^2], \quad (2.5)$$

where $H[0]\,|\, m \,\rangle = E_m |\, m \,\rangle$. Taking the second derivative of the perturbed ground-state energy $E_0[\Phi] = \langle\, 0[\Phi] \,|\, H[\Phi] \,|\, 0[\Phi] \,\rangle$ with respect to the flux up to second order in Φ results [39, 40]

$$\left. \frac{\partial^2 E_0}{\partial \Phi^2} \right|_{\Phi=0} = -\frac{1}{L^2} \langle\, 0 \,|\, \hat{T} \,|\, 0 \,\rangle - \frac{2}{L^2} \sum_{m \neq 0} \frac{|\langle\, 0 \,|\, \hat{j} \,|\, m \,\rangle|^2}{E_m - E_0} = \frac{D}{\pi L}, \quad (2.6)$$

where the last identification follows immediately from the finite-temperature expression eq. (1.24). The Drude weight is thus determined by the curvature of the ground-state energy induced Φ.

We finish this section with some remarks: first note that in the derivation above we have implicitly assumed $E_0[\Phi]$ is minimum at $\Phi = 0$. When this is not the case D should be computed at the minimum of $E_0[\Phi]$ for it essentially describes an equilibrium state among the charge carries within the ring [41, 42]. Second, since the magnetic flux simply produces a phase change Φ when a particle goes around the ring, eq. (2.6) suggests D can alternatively be understood as a measure of the sensitivity of the ground state to a small twist Φ in the boundary conditions. Intuitively if E_0 varies with Φ what happens at the boundaries affects the bulk. This can only be true if the many-body wave function extends coherently throughout the ring, i.e. if the the system is a metal. Therefore the Drude weight yields a simple way of distinguishing metallic from insulating phases [39]. Finally, we point out that the superfluid density is defined very similarly as the Drude weight in eq. (2.6). Specifically, it corresponds to calculating first the ground-state energy in the thermodynamic limit and then its second derivative with respect to the flux [43]. In (quasi) one-dimensional systems D and the superfluid density are therefore equal due to the finite number of energy level crossings in the thermodynamic limit [43, 44]. Thus our results for the Drude weight may also be interpreted as a measure of the superfluid density in the system.

2.2 Numeric computation of the Drude weight

We compute the Drude weight by approximating the second derivative in eq. (2.6) with the finite difference

$$D = \pi L \frac{\partial^2 E_0}{\partial \Phi^2}\bigg|_{\Phi=\Phi_0} \approx 2\pi\, L \frac{E(\Phi) - E(\Phi_0)}{(\Phi - \Phi_0)^2}, \tag{2.7}$$

where Φ_0 is the flux at which the ground-state energy is minimum.

To evaluate eq. (2.7) one needs only the ground-state energy of two L-site rings, one threaded by Φ_0 and the other by Φ. This simplifies matters quite a bit, as compared to what would mean to directly evaluate eq. (2.6) where the entire spectrum is needed. We implemented Lanczos algorithm wherein the entire Hamiltonian matrix H is iteratively projected onto its so-called Krylov subspaces to build a significantly smaller secondary matrix whose eigenvalues approximate (to machine precision) the eigenenergies near the edges of the spectrum of H [45]. Using this technique we compute the lowest eigenvalue of (1.27) for rings of length $L \leq 26$ whose matrix representations in real space have linear dimension of about 10^7 for the largest chain.[2]

Given that the second derivative in eq. (2.7) is to be evaluated at the location where the ground-state energy $E(\Phi)$ is minimum, the dependence of the many-body energy levels on the flux deserves some explanation. In the absence of J_2 the hardcore boson model — XXZ model in the spin notation, is exactly solvable and its Drude weight may be written in closed form [40]. The model may also be Jordan-Wigner transformed into a system of spinless electrons and most results from the bosonic model transfer to the fermionic one [46]. However when a flux Φ threads the ring of electrons, the energy is minimum either at $\Phi_0 = 0$ or π depending on whether the number N of electrons on the ring is odd or even, respectively. Such an energy shift is due to the statistical phase that arises when an electron goes around the ring, thereby changing its place with the other $N-1$ electrons. Such a "parity" effect does not arise in the corresponding hardcore bosonic system whose many-body wave function is symmetric under particle interchange. The energy minimum is thus at $\Phi_0 = 0$ and this is the point about which eq. (2.7) is evaluated. The location of the energy minimum when J_2 is included has also been found to be at $\Phi_0 = 0$, provided the system is not in the incommensurately bond-ordered phase found in [31]. In the left panel of Fig. 2.1 we show a representative plot of the flux dependence of the first three energy levels, for a 16-site two hardcore-boson system, with parameters $J_2 = 0.2\, J_1$ and $\Delta = J_1/2$. Note the energy crossing at $\Phi = \pi$ which results in a jump discontinuity of the persistent flow. Also note the energy levels — as well as all physical properties — are periodic functions of Φ with period 2π.

The right panel of Fig. 2.1 shows the Drude weight for a 20-site half-filled ring and three values of J_2 as a function of nearest-neighbor interaction Δ. It clearly bears out the expected asymmetry with respect to the sing of J_2. Indeed adding an unfrustrated hopping ($J_2 < 0$) simply enhances the Drude weight of the system. The latter is found to monotonically decay with

[2] When these computations were carried out our implementation did not take advantage of translational symmetry. Using the basis of single-particle momentum eigenstates together with Lanczos algorithm one can easily reach larger system sizes.

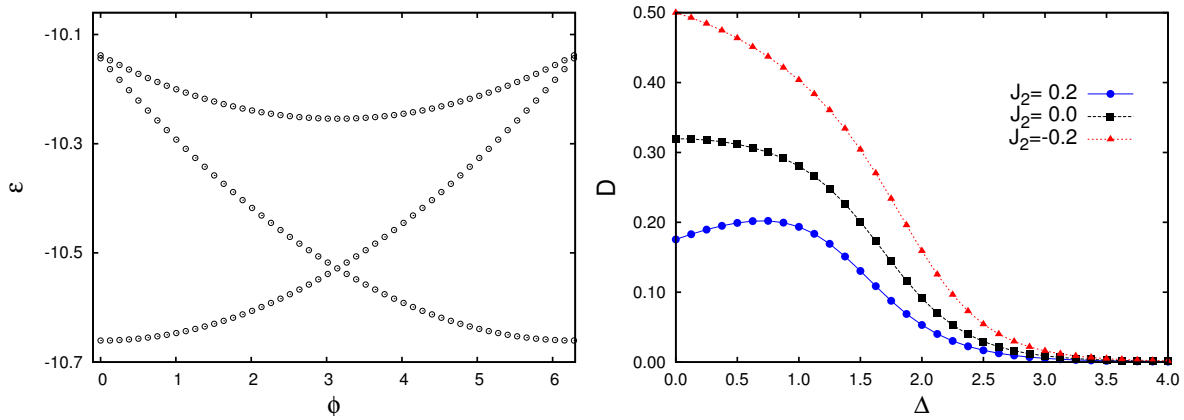

Figure 2.1: *Left panel*: Energy levels as a function of flux in a 16-site ring with two hard-core bosons and system parameters $J_2/J_1 = 0.2$ and $\Delta/J_1 = 0.5$. *Right panel*: Drude weight for a 20-site ring and three values of J_2 as a function of the anisotropy Δ.

increasing the interaction for $J_2 \leq 0$, reflecting the fact that Δ is the only localizing mechanism present. In contrast, frustrated chains displays a nonmonotonic increase in the Drude weight as the repulsive interaction is increased. Before discussing further the physics behind the observed interaction-induced enhancement of D, let us show it corresponds to a thermodynamic effect.

2.3 Finite-size extrapolation and thermodynamic limit

A transition from a superfluid to a charge density wave phase is expected as the nearest-neighbour repulsive interaction strength Δ is increased, and this is true whether J_2 is present or not [30, 40]. In the latter case the Berezinskii-Kosterlitz-Thouless (BKT) transition point is known to be exactly at $\Delta = J_1$ for a half-filled system. On the other hand, in the presence of J_2 the BKT transition points have been computed numerically from the behavior of the single particle excitation gap using the density matrix renormalization group technique [30]. Here we focus on the conducting phase of the system at half-filling and consider the representative frustrated value of $J_2 = 0.2\,J_1$ for which the phase transition was predicted to occur at $\Delta_c \approx 0.7\,J_1$. Our main results are summarised in Fig. 2.2 for a range of system lengths. As expected from previous works [39, 41, 47, 48], we find the Drude weight to scale polynomially $D(L) = D + a/L + b/L^2$ within the conducting phase and exponentially $D(L) = C\exp(-L/\xi)$ within the insulating phase, where the localisation length ξ diverges at the transition, as shown in the right panel of Fig. 2.2. Let us point out we do not employ the scaling laws to identify the transition point. Instead, we assume the transition takes place at $\Delta_c = 0.7\,J_1$ and perform a polynomial extrapolation to the thermodynamic limit of the computed Drude weights for $\Delta < \Delta_c$. Such an extrapolation, shown as a full line in the left panel of Fig. 2.2, works well both for $J_2 = 0.2\,J_1$ and for the exactly solvable $J_2 = 0$ case (inset of figure, showing agreement of the extrapolation with Bethe Ansatz results [40]). For a finite J_2 a similar sharp jump in the Drude weight should occur as $L \to \infty$. This expectation is borne out from our plots.

The most important feature of the data shown in Fig. 2.2 is the rise of the Drude weight as the

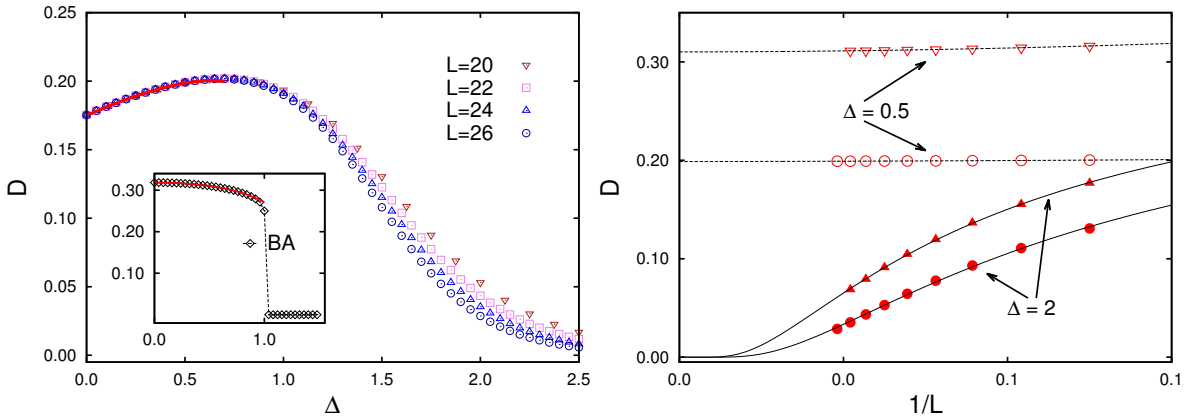

Figure 2.2: Drude weight of half-filled bosonic rings for various chain lengths L. *Left panel*: non-monotonicity of the Drude weight with increasing interaction for frustrated nearest-neighbour hopping $J_2 = 0.2\,J_1$, and polynomial extrapolation (full lines) from data for $L = 20, 22, 24$ and 26 in the conducting phase. Inset shows results from a similar extrapolation for $t_2 = 0$ compared to Bethe Ansatz (BA) results. *Right panel*: scaling of the Drude weight for $J_2 = 0$ (triangles) and $J_2 = 0.2\,J_1$ (circles) as a function of inverse system length for interaction strengths $\Delta = J_1/2$ (open symbols) and $\Delta = 2J_1$ (closed symbols). Full lines are exponential fits $D(L) = C\exp(-L/\xi)$ and dashed lines are polynomial fits $D(L) = D + a/L + b/L^2$ to the thermodynamic limit $L \to \infty$. The fits for $\Delta = 2$ give a localisation length $\xi \approx 15, 11$ for $J_2 = 0, 0.2\,J_1$ respectively. As Δ decreases the fits give increasing estimates for the localisation lengths ξ.

nearest-neighbour interaction is increased, which translates as an enhancement of the persistent flow in the ring. Kinetic (in-plane) frustration favors a situation in which the hardcore bosons gain kinetic energy by hopping back and forth between a pair of nearest-neighbour sites and decoupling from the rest of the system. The repulsive nearest-neighbour interaction Δ favors instead a charge density wave like ordering wherein the particles tend to avoid sitting next to each other. Thus, initially increasing Δ causes a spread of the particles and a concomitant increase in charge density wave fluctuations, which in turn reduces the effective frustration, thereby increasing the Drude weight. However, upon further increase of Δ the insulating behavior dominates and the Drude weight accordingly drops. Crucially, as seen in Fig. 2.2, such a scenario of interaction-induced enhancement of D is valid for finite rings as well as in the thermodynamic limit. This result is in fact more generic and we have checked its validity away from half-filling. The main difference in that case being a much more gradual decay of the Drude weight after it reaches its maximum, which is presumably due to the absence of an insulating phase away from half-filling.

CHAPTER 3

Spin stiffness anomalies: role of symmetries and ensembles

In this chapter we investigate high-temperature ballistic transport in the integrable limit of our model (1.27). Specifically, we use exact diagonalization to compute the spin stiffness in the anisotropic XXZ chain for different combinations of the conserved symmetries and statistical ensembles.

It is well known that both discrete and dynamical symmetries of the model play an important role in the exact-diagonalization calculation of D [49, 50]. We were originally motivated to revisit this long-studied problem due to certain inexplicable ensemble-dependent convergence rates of the finite-system data to the thermodynamic limit, found for certain interaction strengths only [29, 51, 52] — the details will be presented along the way. To resolve these issues we start by systematically enlisting the contribution of the current carrying states in each symmetry sector. In so doing we find what ensemble and what system symmetries (parity, spin-inversion, loop algebra) best help to achieve quickest convergence to the thermodynamic limit. In particular we shall identify the sl_2-loop algebra degenerate states to play an important role in contributing to the thermodynamic limit of the stiffness. This last point is particularly relevant in light of the recent exact bounds to the high-temperature spin stiffness built from noncompact representations of the sl_2-loop algebra [26].

3.1 High-temperature spin stiffness

In chapter 1 we derived an expression for the finite-temperature spin stiffness, namely eq. (1.24). A straightforward generalization of the calculation we presented in section 2.1 to finite temperatures shows the spin stiffness can equivalently be expressed as the thermal average of energy-level curvatures with respect to a fictitious flux Φ threading the L-site periodic spin chain

$$D = \frac{\pi}{L} \sum_n \frac{e^{-\beta E_n}}{Z} \frac{\partial^2 E_n}{\partial \Phi^2}\bigg|_{\Phi=0}, \tag{3.1}$$

where β is the inverse temperature, E_n labels the eigenstates of the unfluxed model and Z is the

partition function [53]. Evaluating the second derivative of the free energy F with respect to the flux, and using eq. (3.1), one immediately finds

$$\left.\frac{\partial^2 F}{\partial \Phi^2}\right|_{\Phi=0} = \frac{L}{\pi} D - \beta \sum_n \frac{e^{-\beta E_n}}{Z} \left(\left.\frac{\partial E_n}{\partial \Phi}\right|_{\Phi=0} \right)^2 + \beta \left(\sum_n \frac{e^{-\beta E_n}}{Z} \left.\frac{\partial E_n}{\partial \Phi}\right|_{\Phi=0} \right)^2 . \tag{3.2}$$

Now we know from eq. (2.4)

$$\left.\frac{\partial E_n}{\partial \Phi}\right|_{\Phi=0} = \langle\, n \,|\, \hat{j} \,|\, m \,\rangle, \quad \text{with } E_m = E_n, \tag{3.3}$$

where the $|\, n \,\rangle$ are eigenstates of the unfluxed model. It follows the quantity within brackets in the last term on the right hand side of eq. (3.2) simply vanishes due to parity. We also know from our discussion in section 2.1 that the first derivative of the Free energy with respect to the flux is proportional to the persistent currents in the system. However, at finite temperatures the XXZ model shows no persistent current and thus $\partial^2 F/\partial \Phi^2|_{\Phi=0}$ vanishes in the thermodynamic limit. Eq. (3.2) thus simplifies to

$$D = \pi \beta \sum_n \frac{e^{-\beta E_n}}{LZ} \sum_{m,\, E_m = E_n} |\langle\, n \,|\, \hat{j} \,|\, m \,\rangle|^2, \tag{3.4}$$

Eq. (3.4) allows us to give an alternative, perhaps more physical, interpretation to the spin stiffness as the long-time asymptotic value of the current-current correlation function. Indeed

$$\lim_{\tau\to\infty} \frac{1}{\tau} \int_0^\tau dt\, \langle\, \hat{j}(t)\, \hat{j}(0) \,\rangle = \frac{L}{\pi\beta} D + \lim_{\tau\to\infty} \frac{1}{\tau} \int_0^\tau dt \left[\sum_n \frac{e^{-\beta E_n}}{Z} \sum_{m,\, E_m \neq E_n} |\langle\, n \,|\, \hat{j} \,|\, m \,\rangle|^2 e^{i(E_n - E_m)t} \right], \tag{3.5}$$

where $\langle\, \cdot \,\rangle$ on the left hand side denotes a thermodynamic equilibrium average and the second term on the right hand side vanishes in the long-time limit. Indeed, the left panel of Fig. 3.1 shows the integrand of this term — which we call $C(t)$ — as a function of time for different system sizes. The black points correspond to spin chains where parity, spin-inversion and loop-algebra symmetries are present, whereas the red points correspond to chains where these symmetries are broken. The main aspect to notice at this stage is that the time integral of $C(t)$ is clearly finite and thus its long-time average vanishes.

In the following we shall numerically evaluate Eq. (3.4) for the XXZ Heisenberg chain in the high-temperature limit, where the meaningful quantity is $\lim_{\beta\to 0} \beta^{-1} D$.

3.2 Quantum loop-algebra degeneracies

Besides the global symmetries discussed in section 1.2.1, the periodic XXZ chain has additional symmetries at the dense set of commensurate “roots of unity" anisotropies $\tilde{\Delta}_{MN} = \cos(\pi M/N)$, with $N \in \mathbb{Z}^+$ and $M < N$ coprimes, for which there exists a large class of zero-energy N-particle excitations [54, 55]. These excitations give rise to degeneracies between a parent state with

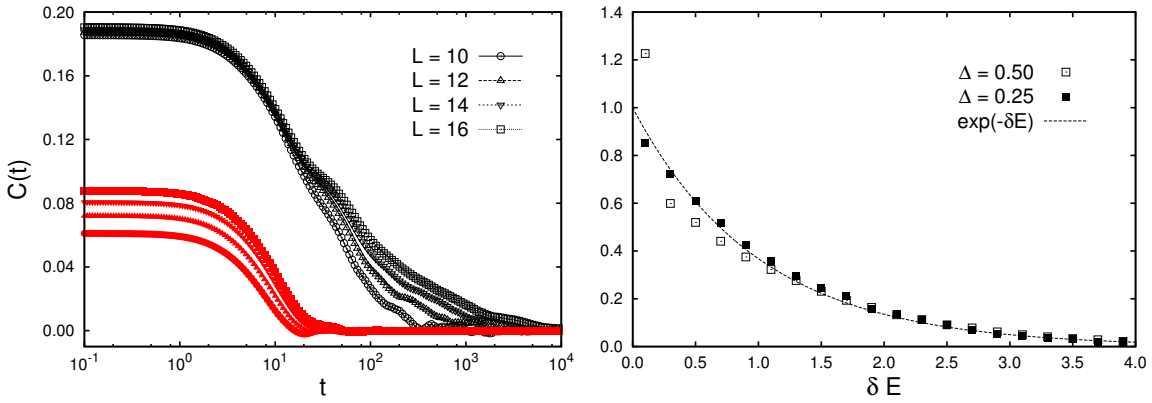

Figure 3.1: *Left Panel*: time dependence of the correlation function $C(t)$ — the integrand of the second term on the right hand side of eq. (3.5) — for $\Delta = 0.25$. The black points correspond to spin chains where parity, spin-inversion and loop-algebra symmetries are present, whereas the red points correspond to chains where these symmetries are broken. *Right panel*: XXZ 20-site chain level-spacing distribution for states within the sector of zero total magnetization, for two different anisotropies. The distribution is averaged over each spin-inversion sector z, for every crystal momentum, as well as over parities for $K = \{0, \pi\}$. Note the peak at $\delta E = 0$ for $\Delta = 0.5$ signaling the presence of additional degeneracies.

$m_z = m_z^{\max}$ and states with $m_z = m_z^{\max} - l\,N$, where $l \in \mathbb{Z}^+$. Deguchi et al. [54] numerically studied these degeneracies and found the corresponding multiplets have multiplicity

$$\begin{pmatrix} 2\,m_z^{\max}/N \\ l \end{pmatrix}, \tag{3.6}$$

in the commensurable case $m_z = 0 \pmod N$, and

$$\begin{pmatrix} 2\,[m_z^{\max}/N] + \alpha \\ l \end{pmatrix}, \tag{3.7}$$

in the incommensurable case $m_z \neq 0 \pmod N$, where $[x]$ denotes the greatest integer contained in x, and $\alpha = 0, 1$ or 2. In particular, the degeneracies in the commensurable case were related to the sl_2-loop algebra [54], whose generators commute with the XXZ Hamiltonian at roots of unity when $m_z = 0 \pmod N$. However the incommensurable sectors do not have this symmetry. We shall refer to the quantum symmetry in the full Hilbert space by Λ henceforth.

The additional degeneracies in the system at these special $\tilde{\Delta}_{MN}$ points can be readily verified by inspecting its level-spacing distribution [56]. To find the latter one first needs to *unfold* the eigenenergies so as to make the density of states constant throughout the spectrum [10]. The unfolded eigenenergies $\tilde{E}_n$ are usually defined through the average integrated density of states $\langle N(E)\rangle$ as $\tilde{E}_n \equiv \langle N(E_n)\rangle$, with

$$N(E) = \sum_m \Theta(E - E_m), \tag{3.8}$$

where the summation runs over all the eigenenergies of the model and $\Theta(E)$ denotes the Heaviside step function. We approximate the average $\langle N(E)\rangle$ with a spline interpolation through

a set of equidistant points within the bandwidth.

Now, being an integrable model the XXZ chain has a macroscopic number of conserved quantities which fully diagonalize the Hamiltonian. The resulting eigenvalues are statistically uncorrelated and their spacing distribution follows a Poisson distribution. In contrast, as shown in the right panel of Fig. 3.1, at the commensurate anisotropy $\Delta = \tilde{\Delta}_{1,3} = 0.5$ the level spacing distribution deviates from the Poisson distribution and displays a small peak at $\delta E = 0$ signaling the presence of additional degeneracies.

3.3 Current-carrying states in the XXZ model

Given that $\hat{m}_z$ commutes with $\hat{K}$, these two symmetry operations can be used to block-diagonalize the XXZ model. The resulting eigenstates can then be labeled by both the total magnetization m_z and the total crystal momentum K. On the other hand, the discrete symmetries can only be used for block diagonalization in specific subsectors [57]: (i) $\hat{Z}$ commutes with both $\hat{P}$ and $\hat{K}$ but only does so with $\hat{m}_z$ in the sector with zero total magnetization; (ii) $\hat{P}$ commutes with $\hat{m}_z$ but with $\hat{K}$ only in the subsectors with zero and π total crystal momentum. Now, the numerical evaluation of eq. (3.4) may be performed either in the canonical or grand canonical ensemble. In the former case we sum over eigenstates with a fixed total magnetization m_z, whereas in the latter the summation includes eigenstates from all the different magnetization sectors. In what follows we consider only spin chains with *e*ven L.

Let us start by summarizing a couple of empirical observations regarding the many-body states connected by the current operator (1.32) when the spin stiffness is evaluated within the canonical ensemble. To study how parity and spin-inversion enter in the determination of the stiffness, we break them using an irrational magnetic flux $\Phi = \sqrt{2}$. The effect of threading the periodic chain with a flux is incorporated into the model by gauging Φ into the spin-ladder operators via the usual Peierl's substitution (2.2). The flux also lifts every $\tilde{\Delta}$-related degeneracy, as we expatiate more fully below.

We shall see that when parity and spin-inversion symmetries are broken all nondegenerate eigenstates of the XXZ model are eigenstates of the spin current operator, and that the main contribution to the spin stiffness comes precisely from these nondegenerate states ($m = n$) — the degenerate states being only those coming from the Λ quantum symmetry at $\tilde{\Delta}_{MN}$. By contrast, if spin-inversion is present only Λ-related degenerate states contribute to D *provided* $L \geq 2N$. Table 3.1 recaps the main points we discuss below.

3.3.1 $m_z = 0$ Sector

Due to the discrete symmetries present in this subsector, and to the oddness of the spin current under their action, only matrix elements from degenerate states of the form

$$\langle\, m, K, z \,|\, \hat{j} \,|\, -z, K, n \,\rangle, \quad \text{with} \quad K \neq \{0, \pi\}, \tag{3.9}$$

or

$$\langle\, m, K, z, p \,|\, \hat{j} \,|\, -p, -z, K, n \,\rangle, \quad \text{with} \quad K = \{0, \pi\}, \tag{3.10}$$

Symmetry	**C**urrent carrying states
$\hat{Z}$, $\hat{P}$ and Λ $\hat{Z}$ and Λ	Degenerate multiplets from Λ symmetry only.
$\hat{P}$ and Λ	All pairwise degenerate states of different parity, including Λ multiplets.
$\hat{Z}$ and $\hat{P}$ $\hat{Z}$	None.
$\hat{P}$	All pairwise degenerate states of different parity.
Λ	Every nondegenerate state, and the degenerate Λ multiplets.
None	Every nondegenerate state.

Table 3.1: Current carrying states for symmetry blocks with fixed (m_z, K) and different combinations of spin-inversion $\hat{Z}$, parity $\hat{P}$, and quantum-loop Λ symmetries.

and $E_n = E_m$ contribute to the spin stiffness (3.4).

For anisotropy values different from $\tilde{\Delta}_{MN}$ we find degenerate states only within the sectors of $K = \{0, \pi\}$. These states belong to different parity sectors but have the same spin-inversion signature and hence are not connected by the current operator. Therefore, there is no net current for any L and the stiffness vanishes exactly in the sector of zero total magnetization. Note that at the isotropic point ($\Delta = 1$) the SU(2) symmetry was exploited to show explicitly that $D = 0$ for any β [27].

For $\Delta = \tilde{\Delta}_{MN}$ we find degenerate states due to the additional Λ symmetry only for chain lengths

$$L \geq L_{\min} \equiv 2N, \tag{3.11}$$

the number of which increases with system size. Indeed Λ-related spectral degeneracies are split between sectors of $m_z = 0 \pmod N$ [54]. These have multiplicities given by (3.6) and the minimum length (3.11) for which we start finding such degeneracies follows precisely from that equation. Given $m_z^{\max} = L/2$ one finds the symmetry sectors with total magnetization $m_A = L/2 - N$ and $m_B = m_z^{\max}$ are degenerated. Each of these sectors has the smallest Λ-related degenerate subspace possible whose dimension is L/N. It immediately follows that for system sizes $L = 2N$ one should find the first pair of Λ-degenerate states within the $m_z = 0$ sector. Such a pair is also degenerate with a second pair belonging to the sector of $m_z = N$. We have checked numerically this is indeed the case, and table 3.2 shows an example. Importantly, these states are pairwise degenerate with opposite spin-inversion — as well as opposite parity within the $K = \{0, \pi\}$ sectors — and yield a finite spin stiffness. We remark this is the only case where degenerate contributions to D dominates over the nondegenerate contributions.

L	deg($\Delta = 0.25$)	deg($\Delta = \tilde{\Delta}_{16}$)
8	4	4
10	20	20
12	96	98
14	364	392
16	1364	1592

Table 3.2: Number of degenerate states in the sector of zero total magnetization, for different system sizes and two anisotropy values. Note how the first two degenerate states due to the Λ symmetry appear at $L = 2N = 12$.

3.3.2 $m_z \neq 0$ Sector

In the sectors of finite total magnetization there is no spin-inversion symmetry and hence every state potentially carries a current. The relevant matrix elements are now

$$\langle m, K \,|\, \hat{j} \,|\, K, n \rangle, \quad \text{with} \quad K \neq \{0, \pi\}, \tag{3.12}$$

or

$$\langle m, K, p \,|\, \hat{j}^z \,|\, -p, K, n \rangle, \quad \text{with} \quad K = \{0, \pi\}, \tag{3.13}$$

with $E_n = E_m$. For $\Delta \neq \tilde{\Delta}_{MN}$ and $K = \{0, \pi\}$, we find pairwise degenerate states of opposite parity, each of which are connected through the spin current operator. The rest of the K-subsectors have no degenerate states, but all of these are found to be eigenstates of the current operator and, consequently, to carry a finite current. Since all K sectors are about the same dimension, it follows that nondegenerate current-carrying states yield the dominant contribution to the spin stiffness, an observation which has been made before [50]. For $\Delta = \tilde{\Delta}_{MN}$ one finds additional degeneracies in all K-subsectors. These additional degenerate states are not eigenstates of the current but do contribute to the spin stiffness through off-diagonal terms.

3.3.3 $m_z = 0$ Sector and finite magnetic flux

If $\Delta \neq \tilde{\Delta}_{MN}$ and $K = \{0, \pi\}$ we find the same number of degenerate states as for the non-fluxed model. In this case, however, since parity and spin inversion are broken degenerate and nondegenerate states alike give finite contributions to the summation in eq. (3.4). For all the other momenta one finds that all states are nondegenerate eigenstates of $\hat{j}^z$ and carry a finite current. Summarizing, the relevant matrix elements in this case are

$$\langle m, K \,|\, \hat{j} \,|\, K, n \rangle \, \delta_{mn}, \quad \text{with} \quad K \neq \{0, \pi\}, \tag{3.14}$$

or

$$\langle m, K \,|\, \hat{j} \,|\, K, n \rangle, \quad \text{with} \quad K = \{0, \pi\}, \tag{3.15}$$

with $E_n = E_m$. Remarkably, if $\Delta = \tilde{\Delta}_{MN}$ we find the presence of the flux lifts all the extra degeneracies coming from the additional quantum symmetry and hence the model behaves as though $\Delta \neq \tilde{\Delta}_{MN}$.

3.3.4 $m_z \neq 0$ Sector and finite magnetic flux

In this last case we find no degenerate state in any of the symmetry subsectors, and that all the eigenstates of the model are also eigenstates of the current operator, and carry a finite current regardless of Δ. All contributing matrix elements, within any K-sector, therefore are of the form

$$\langle m, K \,|\, \hat{j} \,|\, K, n \rangle \, \delta_{mn}. \tag{3.16}$$

3.4 Finite-size spin stiffness anomalies

We present our infinite temperature spin stiffness results in Fig. 3.2, evaluated within the grand canonical (GCE) and canonical ensemble (CE) in the $m_z = 0$ sector, both with and without a flux, for even-length chains of size $L = 6 - 18$. We also show a second order $(1/L)$-polynomial fit to the data points of $L = 10 - 18$ to guide the eye.

Per usual statistical mechanics GCE and CE should be equivalent in the thermodynamic limit, especially if the quantity measured is a meaningful one in this limit [58]. We will find that although in the gapped phase D quickly becomes independent of both ensemble and symmetries as L increases, in the gapless phase the presence of spin-inversion symmetry makes convergence towards the thermodynamic limit remarkably slow, depending on how fast the Λ degeneracies start showing up when increasing system size.

3.4.1 Gapless phase

For $\Delta < 1$ it is rigorously known that the high temperature transport is ballistic [60] i.e. $D > 0$ in *any* magnetization sector, especially the zero magnetization sector where Mazur's inequalities alone do not settle the issue. However computing the actual value of D in the gapless phase is a different matter, with D lower-bounded more strictly recently [26], and even claimed to be exactly computable [59]. The explicit expression for the exact bound at the $\tilde{\Delta}_{MN}$ points reads

$$D \geq 2\pi \frac{\beta}{16} \frac{\sin^2(\pi M/N)}{\sin^2(\pi/N)} \left(1 - \frac{N}{2\pi} \sin(2\pi/N)\right). \tag{3.17}$$

In the top panels of Fig. 3.2 we show the finite size data for $\beta^{-1}D$ as a function of system size in the gapless phase, for two anisotropies $\Delta = 0.25, 0.50$ – the latter being the Λ-symmetric point $\tilde{\Delta}_{1,3}$. In both cases we note (i) D always extrapolates in the thermodynamic limit to a finite value $O(1)$ and (ii) the fluxed cases, for finite L, always gives larger D values. The second point is analogous to the observation that in the GCE odd-length chains have larger D values than even-length chains[29]. The reason behind such a difference lies mainly in the presence/absence of spin-inversion symmetry — for odd-length chains spin-inversion is always broken. Indeed, as pointed out above, in the absence of spin-inversion all eigenstates, whether degenerate or not, of the XXZ Hamiltonian are connected by the current operator and give a finite contribution to D. If the states have a definite z-signature, in contrast, many of the eigenstates of H, as e.g. all states with $m_z = 0$ for $\Delta \neq \tilde{\Delta}_{MN}$ carry no current. Hence D assumes greater values in the GCE for either fluxed or odd-length periodic chains.

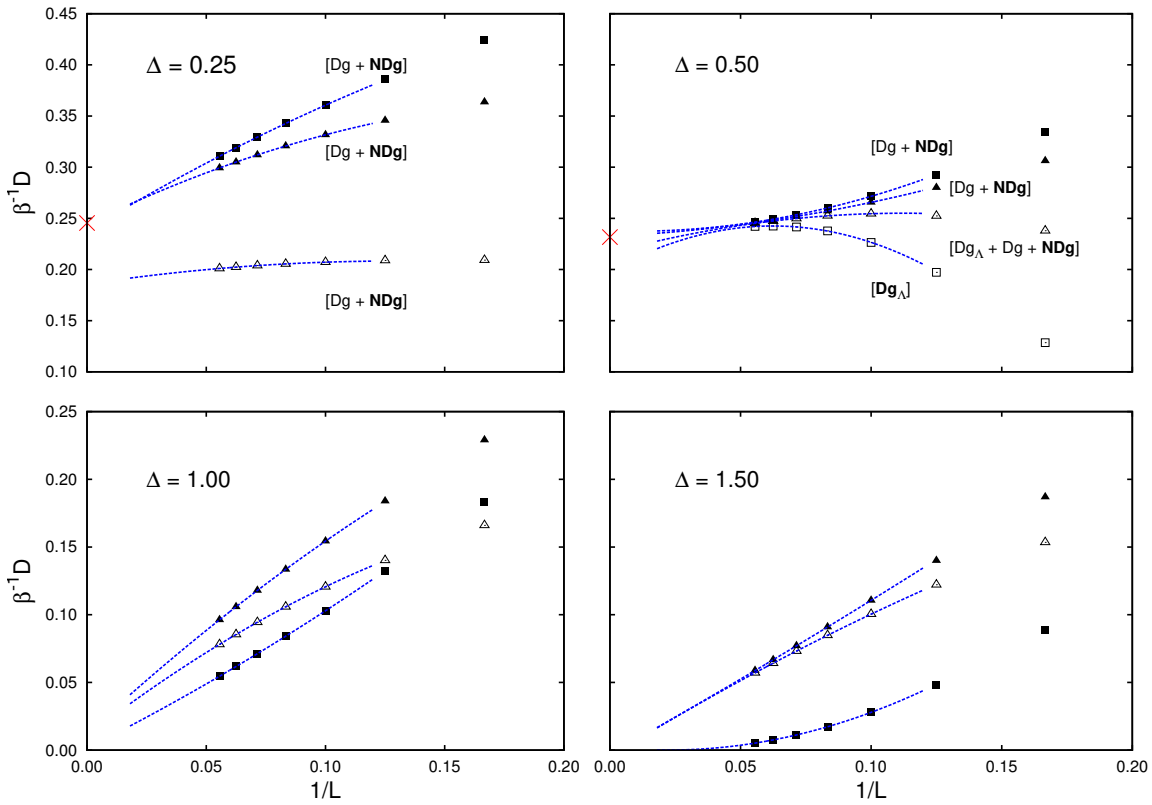

Figure 3.2: Finite size scaling of the spin stiffness for different values of the anisotropy Δ, calculated within both canonical (CE) and grand canonical ensemble (GCE), and in the presence and absence of a magnetic flux. Symbol coding: ▲ GCE with flux, △ GCE without flux, ■ CE with flux and □ CE without flux. The dashed lines correspond to second order polynomial fits and are to be taken as guide to eye. Top panels show results for the gapless phase, with the crosses representing exact results in the thermodynamic limit [26, 59], and the type of current carrying states that contribute to the finite-L D values labeled as nondegenerate (NDg), degenerate (Dg), and Λ-degenerate states (Dg_Λ); the dominant contributor is highlighted in bold. Bottom panels show results away from gapless phase, consistent with vanishing spin stiffness for $L \to \infty$, independent of ensemble or symmetry.

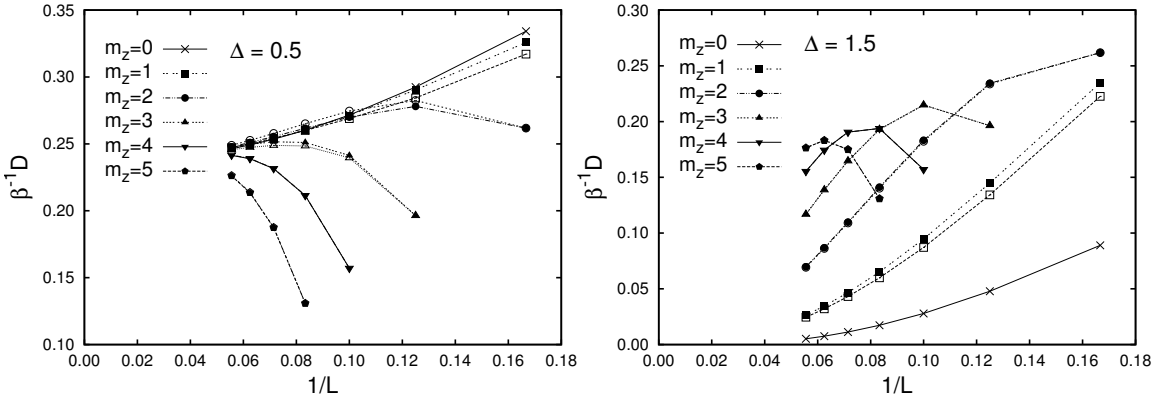

Figure 3.3: Finite size scaling of the spin stiffness in the canonical ensemble for two Δ values, calculated in the presence (full symbols) and absence (empty symbols) of a magnetic flux, for different magnetization sectors. Crosses indicate $m_z = 0$ values in the presence of a flux. As m_z and L increase the effect of flux disappears for both anisotropies; however note that for larger Δ the $m_z = 0$ contributes the least, whereas it is the opposite for smaller Δ, explaining why, when the weighted average is taken, $m_z = 0$ CE is above (below) the GCE result as seen in the upper (lower) right panel of Fig. 3.2 for the two anisotropies. Note that our D computation is for fixed m_z (rather than m_z/L) and hence the tendency to extrapolate to zero, as well as the nonmonotonicity at large L seen in the top figure.

Let us focus on $\Delta = 0.5$ first. We see that independent of keeping or breaking the discrete symmetries and the type of ensemble chosen, the D values always agree with one another, even for moderately small $L \approx 18$. Pivotally, they tend to extrapolate to the same value in the thermodynamic limit which is in good agreement with the exactly computed lower bound [26, 59], marked with a cross in the figure. Note that for $\Delta = 0.5$ the lower bound, eq. (3.17), and our numerics of Fig. 3.2, also agree with the Thermodynamic Bethe Ansatz (TBA) solution [51, 61, 62]

$$\beta^{-1} D = 2\pi \frac{\gamma - \sin(2\gamma)/2}{16\gamma}, \tag{3.18}$$

with $\gamma = \cos^{-1}(0.5) = \pi/3$.

For the second case of $\Delta = 0.25$, which is not *exactly* equal to one of the $\tilde{\Delta}_{MN}$ points (although it can come arbitrarily close to one) the results seem generally the same but distinctly different in one aspect: the finite-size data for the GCE without flux seems to extrapolate to a different thermodynamic limit from the fluxed GCE or CE cases. The latter two here tend to extrapolate to the same thermodynamic limit in good agreement with the exactly lower-bounded result [26]. We understand the source of the discrepancy between non-fluxed GCE and fluxed GCE/CE – as well as to theoretical predictions – as follows: consider the nearby Λ symmetric point $\tilde{\Delta}_{13,31} = \cos(13\pi/31) \approx 0.2506$. For the system sizes considered here the difference $D[\Delta = 0.25] - D[\tilde{\Delta}_{13,31}]$ is always of the order of 10^{-4}. However, we know from the previous section that for $\tilde{\Delta}_{13,31}$ the degeneracies due to the Λ symmetry start showing up for spin chains of length $L \geq 2 \times 31 = 62$. We also know that these degenerate states, the number of which increases with system size, carry a finite current. Thus in order to see the GCE non-fluxed data for $\tilde{\Delta}_{13,31}$ extrapolate to the exact result one would have to consider chains of length $L \geq 64$.

Such system sizes are out of the question when all exact eigenstates are needed.

Going back to the $\Delta = 0.5$ example, the degeneracies from the Λ symmetry are already present for chains of length $L \geq 6$. This is why we see how, when increasing system size, both non-fluxed GCE and CE data approach the exact lower bound from below. The problem with $\Delta = 0.25$ is that as one chooses $\tilde{\Delta}_{MN}$ points closer to it, the integer N gets significantly large and the corresponding $D[\tilde{\Delta}_{MN}]$ converges towards its exact value very slowly. This of course does not answer the question whether the actual (non-fluxed) GCE data at exactly $\Delta = 0.25$, or any $\Delta \neq \tilde{\Delta}_{MN}$ for that matter, where no Λ symmetry is present, converges towards some (M, N)-dependent lower bound.

We close this subsection with the following remark: we have noticed that when increasing the anisotropy, the contribution to the spin stiffness from the symmetry sectors of larger magnetization densities slowly start dominating the summation in eq. (3.4), as exemplified by Fig. 3.3 for $\Delta = 1.5$ (top panel), whereas the trend is exactly the opposite for the smaller anisotropy $\Delta = 0.5$ (bottom panel). This makes the GCE computation for large Δ less susceptible to the physics of the zero- and low magnetization sectors, and hence to the symmetry-related anomalies. In fact, we have carried out computations for the large anisotropies $\tilde{\Delta}_{1,6} \approx 0.87, 0.9$ and $\tilde{\Delta}_{1,8} \approx 0.92$ and confirmed that, even when the current-carrying Λ-degenerated states have yet to appear, the GCE data extrapolates to the same thermodynamic limit as the fluxed GCE and CE data.

3.4.2 Isotropic point and gapped phase

Away from the gapless phase the high-temperature spin stiffness is expected to vanish [19, 20, 29, 63]. We confirm this picture holds for GCE and CE, again with and without a flux, in the bottom panels of Fig. 3.2. For $\Delta \geq 1$ the quantum symmetry Λ is absent [54, 55] and the non-fluxed CE with $m_z = 0$ case gives once more identically zero D due to spin-inversion (and hence it is not shown). Accordingly the fluxed GCE results, which include finite contributions from the zero magnetization sector, are above the non-fluxed ones. The main difference one notes here, in contrast to the two gapless points from above, is that the $m_z = 0$ CE D values are lower than those for the GCE. This is so because, as already mentioned, for these anisotropies and available system sizes, the contributions from the symmetry sectors of finite magnetization densities dominate the summation in eq. (3.4) (see Fig. 3.3). Thus the GCE results show less dependence on flux, and hence on $\hat{Z}$ and $\hat{P}$ when increasing Δ, as was seen in Fig. 3.2.

3.4.3 Extrapolation anomalies within the gapless phase ($\Delta < 1$)

Despite seemingly good convergence of the numerical results to the lower bound of Ref. [26] when all symmetries are broken, we will see that there are caveats.

Herbrych et al. [51] found that for anisotropies $\Delta > 0.5$ the spin stiffness generically scales as $1/L$ and extrapolates to the TBA result, eq. (4.26). They pointed out, however, that for some anisotropies $\Delta < 0.5$, the spin stiffness does not scale as $1/L$ due to the emergence of finite-size low-frequency contributions in the regular part of the Kubo conductivity, which lead to a finite correction δD in the thermodynamic limit. It was found, in particular, that when such a correction is *n*ot taken into account, the spin stiffness data does not extrapolate to the TBA result.

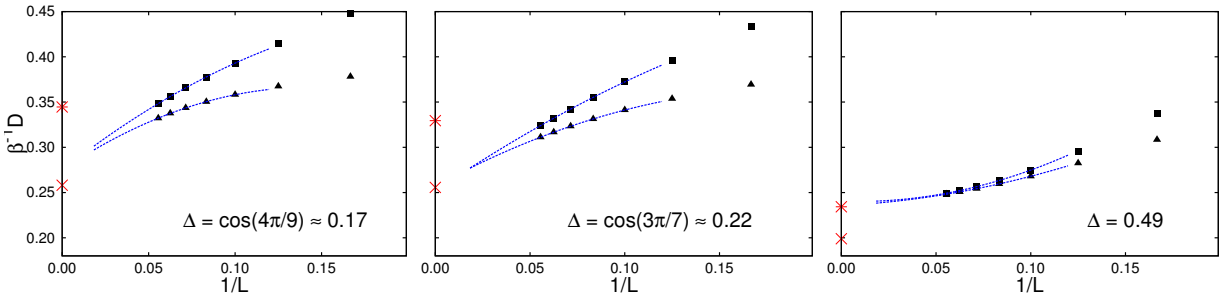

Figure 3.4: Finite size scaling of the spin stiffness computed in both fluxed CE (■) and GCE (▲) within the gapless phase. The crosses represent the exact lower bound results, eq. (3.17), and the stars the Thermodynamic Bethe Ansatz results, eq. (4.26).

Here we complement these observations by reporting that, for those anisotropies where the low-frequency anomalies take place, and if no correction δD is considered, D nicely extrapolates to the exact lower bound, eq. (3.17), as was already seen in the top panel of Fig. 3.2 for $\Delta = 0.25$. Fig. 3.4 shows additional data for the anisotropies $\tilde{\Delta}_{4,9} \approx 0.17$, $\tilde{\Delta}_{3,7} \approx 0.22$ and 0.49. In the left and center panels D clearly extrapolates to the lower bound, marked with a crux. Interestingly, when approaching the point $\tilde{\Delta}_{1,3} = 0.5$ the finite-size data extrapolates instead to the TBA solution, as can be seen in the right panel of Fig. 3.4 for $\Delta = 0.49$ (for any $\tilde{\Delta}_{1,M}$ Eqs. (3.17) and (4.26) agree). Similarly, when approaching $\tilde{\Delta}_{1,2} = 0$ the data again extrapolates to the TBA solution: we have checked this explicitly for $\Delta = 0.05$. We are unable to theoretically account for the convergence to these two distinct results, apart from concluding that (i) the low-frequency anomalies of Ref. [51] seem to vanish when close to the $\tilde{\Delta}_{1,2}$ and $\tilde{\Delta}_{1,3}$ points, and that (ii) in between these points, where the anomalies take place, the data extrapolates to the exact lower bound of Ref. [26].

CHAPTER 4

Anomalous transport in spins-half chains

Within linear response theory, the connection between transport properties and conserved quantities is evident when considering the real part of the Kubo conductivity [22]

$$\sigma'(\omega) = D\,\delta(\omega) + \sigma_{\mathrm{reg}}(\omega), \tag{4.1}$$

where the spin stiffness D can be expressed as a thermal average over the energy level curvatures of the many-body system with respect to a fictitious magnetic flux [53]. A finite spin stiffness thus implies an infinite conductivity and hence ballistic transport.

Integrable models have an infinite set of local conserved quantities which, for some regions of the models' parametric space, couple with the current operator of the relevant dynamical degrees of freedom. The nondecaying components of the current then yield a finite stiffness, and hence ballistic transport, even at infinite temperatures [9, 53]. In contrast generic nonintegrable models show level repulsion and, as a consequence, their energy level fluctuations are bound to a range of the order of the average level spacing which vanishes in the thermodynamic limit. The thermal average over the level curvatures of the model, i.e. the stiffness D, is therefore expected to go to zero when increasing the system's size [53]. Such an expectation is generally borne out by numeric simulations [23]. Thus in nonintegrable models and integrable models with rapidly decaying currents, finite-temperature transport is governed by the regular component of the conductivity, $\sigma_{\mathrm{reg}}(\omega)$, whose low-frequency behavior can be non-analytic due to the nonlinear coupling between collective modes of the conserved degrees of freedom [64], and is usually expected to display normal diffusion, i.e. long-lived modes as independent Gaussian fluctuations, although unconventional low-frequency power-law behavior is still in general possible.

In this chapter we study infinite temperature AC transport in the integrable spin-1/2 XXZ chain, as well as their response to next-nearest neighbor (NNN) integrability breaking spin-flips. Our analysis is based on (i) a three-parameter Ansatz for the memory function whose long-wavelength limit describes the Kubo conductivity, and (ii) an exact-diagonalization evaluation of the regular component of the Kubo formula for small spin chains. The Ansatz is chosen as to capture the possibility of anomalous diffusion at and close to the integrable limit, and yields an expression for the low-frequency power-law exponent of the regular conductivity in terms of the

microscopic parameters of the model.

4.1 Memory function and sum rules

Let us consider the spin correlation function $C_{j,j'}(t)$, defined here as a scalar product in operator space

$$C_{j,j'}(t) = (\hat{S}^z_j|\hat{S}^z_{j'}(t)) \equiv Z^{-1}\mathrm{Tr}\{\,\hat{S}^z_j\hat{S}^z_{j'}(t)\,\}, \tag{4.2}$$

where Z is the partition function and equals the dimension of the Hilbert space, and $\hat{S}^z_j(t) = e^{iHt/\hbar}\hat{S}^z_j e^{-iHt/\hbar}$. This correlation function describes the spontaneous fluctuations of the local magnetization and diverges for asymptotically large times due to the m_z-conservation law.

It is convenient to work with the (lattice) Fourier transform of Eq. (4.2)

$$C(k,t) = \frac{1}{L}\sum_j e^{-ikj}C_{j,0}(t). \tag{4.3}$$

Instead of directly studying the complicated structure of $C(k,t)$ in the long-time limit, we will consider another time correlation function, the so-called memory function [65–67], whose dynamics does not include the intrinsic fluctuations of m_z, nor those of any other slow degree of freedom of the model, for these are explicitly projected out in its construction. In the limit of asymptotically large times one then expects the spectrum of the memory function to be simpler than that of $C(k,t)$, and so that approximations to it have a better chance of success.

4.1.1 Memory function formalism

To construct the memory function we follow Berne and Harp [67] and specialize their generic formulation to integrable systems. Consider the set $\{\hat{Q}_j\}$ of operators describing the slow modes of our model, with $\hat{Q}_0 \equiv \hat{S}^z_k$ the Fourier transform of $\hat{S}^z_i$ and $\hat{Q}_{j>0}$ the (infinite) set of local (or quasilocal) conserved quantities associated with the integrable limit of the Hamitonian (1.27). Note that we do not need to include in $\{\hat{Q}_j\}$ the operator describing the slow energy fluctuations of the system since these do not couple to the magnetization, and hence the set $\{\hat{Q}_j\}$ only includes $\hat{Q}_0$ in the nonintegrable case.

We choose the $\{\hat{Q}_{j>0}\}$ such that

$$(\hat{Q}_i|\hat{Q}_j) = Z^{-1}\mathrm{Tr}\{\,\hat{Q}_i\hat{Q}_j\,\} = \delta_{i,j}\chi_i\beta^{-1}, \tag{4.4}$$

with $\chi_j = \beta(\hat{Q}_j|\hat{Q}_j)$ the static susceptibility associated to $\hat{Q}_j$. Furthermore the $\{\hat{Q}_j\}$ are so chosen that their ensemble averages are zero, that is $\langle Q_j\rangle = Z^{-1}\mathrm{Tr}\,\hat{Q}_j = 0$. The set $\{\hat{Q}_j\}$ can thus be regarded as a set of vectors in a Hilbert space. The projector operator onto the subspace of slow modes follows

$$\hat{P} = \sum_j \beta\chi_j^{-1}|\hat{Q}_j)(\hat{Q}_j|. \tag{4.5}$$

To study the spin dynamics we consider the equation of motion (EOM) $\partial_t|\hat{Q}_0(t)) = iL|\hat{Q}_0(t))$, where L is the *Liouville operator* defined by $iL\hat{O} \equiv -i[\hat{O}, \hat{H}]$. This EOM can clearly be rewritten as

$$\partial_t|\hat{Q}_0(t)) = iL\hat{P}|\hat{Q}_0(t)) + iL(1-\hat{P})|\hat{Q}_0(t)). \tag{4.6}$$

The EOM describing the spontaneous fluctuations of the local magnetization thus follows

$$\partial_t C(k,t) = (\hat{Q}_0|iL\hat{P}|\hat{Q}_0(t)) + (\hat{Q}_0|iL(1-\hat{P})|\hat{Q}_0(t)). \tag{4.7}$$

Now note the first term on the right hand side of eq. (4.7) vanishes since, first, $iL|\hat{Q}_j) = \delta_{0,j}|iL\hat{Q}_j)$ because the $\{\hat{Q}_{j>0}\}$ are constants of motion; and second $(\hat{Q}_0|iL|\hat{Q}_0) = 0$ for $\hat{Q}_0$ is odd under time reversal. The second term on the right hand side of eq. (4.7) can be obtained by acting with $(1-\hat{P})$ on the left of eq. (4.6) and solving for $(1-\hat{P})|\hat{Q}_0(t))$. This yields

$$(1-\hat{P})|\hat{Q}_0(t)) = \sum_j \int_0^t d\tau e^{i(1-\hat{P})L(t-\tau)}(1-\hat{P})iL|\hat{Q}_j)\beta\chi_j^{-1}(\hat{Q}_j|\hat{Q}_0(\tau)). \tag{4.8}$$

Noting only the $j = 0$ contribution from the summation above is finite and that

$$e^{i(1-\hat{P})Lt}(1-\hat{P}) = (1-\hat{P})e^{i(1-\hat{P})L(1-\hat{P})t}, \tag{4.9}$$

we write eq. (4.7) as

$$\partial_t C(k,t) = -\int_0^t d\,\tau(\hat{Q}_0|iL(1-\hat{P})e^{i(1-\hat{P})L(1-\hat{P})(t-\tau)}(1-\hat{P})iL|\hat{Q}_0)\beta\chi_0^{-1}C(k,\tau). \tag{4.10}$$

Finally, using the continuity equation $iL\hat{Q}_0 = -ik\hat{j}_k$, where $\hat{j}_k$ is the Fourier transform of the total spin current (1.32), one can rewrite eq. (4.10) as

$$\partial_t C(k,t) + k^2\int_0^t d\tau\Sigma(k,t-\tau)C(k,\tau) = 0, \tag{4.11}$$

with $\Sigma(k,t)$ the memory function [68] defined here as

$$\beta^{-1}\chi_0\,\Sigma(k,t) = (\hat{j}_k|(1-\hat{P})e^{i(1-\hat{P})L(1-\hat{P})t}(1-\hat{P})|\hat{j}_k), \tag{4.12}$$

From eq. (4.12) we see the memory function differs from the usual current-current correlation function in two aspects [3]: first, the evolution operator determining the spectrum of $\Sigma(k,t)$ has the intrinsic fluctuations of the slow modes $\{\hat{Q}_i\}$ projected out of it; second, only the components of the current orthogonal to the subspace spanned by the $\{\hat{Q}_{i>0}\}$ determine the memory function.

In the long-wavelength limit, however, the projection operation has no effect [3] and so

$$\lim_{k\to 0}\beta^{-1}\chi_0\,\Sigma(k,t) = \lim_{k\to 0}(\hat{j}_k|e^{iLt}|\hat{j}_k)$$
$$= \beta^{-1}\sigma'(t), \tag{4.13}$$

with $\beta^{-1}\chi_0 = (\hat{S}^z_k|\hat{S}^z_k) = 1/4$ and $\beta^{-1}\sigma'(t)$ the infinite-temperature Kubo conductivity.

Eq. (4.13) implies the memory function displays the same behavior as the Kubo conductivity (4.1) in the long-wavelength limit. That the memory function is well behaved as k approaches zero follows since the total spin current operator is a local operator and, consequently, its correlation function falls off rapidly with distance. A bit more subtle is the long-time limit, at which the memory function might become nonanalytic due to, e.g., (i) the aforementioned presence of local or quasilocal conserved quantities coupling to the current, which contribute to $\Sigma(k,t)$ in the long-wavelength limit, or (ii) mode-mode coupling of the conserved spin density [64], which may be relevant even at finite wavevectors [3].

4.1.2 Sum rules

To derive sum rules for the memory function, consider the Laplace-transform of Eq. (4.11)

$$\tilde{C}(k,z) = \frac{i\beta^{-1}}{z + ik^2\tilde{\Sigma}(k,z)}\chi_0, \quad (\mathrm{Im}z > 0), \tag{4.14}$$

and note that in the long-wavelength limit $\tilde{C}(k,z)$ has a pole at $z = 0$ — a direct consequence of the fact that $\lim_{k\to 0} C(k,t)$ does not decay in time. In this limit eq. (4.14) can be expressed as

$$\frac{\widetilde{C}(k,z)}{i\beta^{-1}\chi_0} = \frac{1}{z}\left(1 - i\frac{k^2}{z}\widetilde{\Sigma}(kz) + O[k^4]\right). \tag{4.15}$$

Now, using the representation $2\pi i\tilde{f}(k,z) = \int d\omega f(k,\omega)(\omega - z)^{-1}$ for both $\tilde{C}(k,z)$ and $\tilde{\Sigma}(k,z)$ one can, in the limit of large z, Taylor expand both sides of the dispersion relation (4.15) in z^{-1} and equate the expansion coefficients. One thus obtains a set of identities relating the frequency moments of the spin correlation function with those of the memory function. We write these sum-rules as

$$\mu_n \equiv \frac{1}{k^2}\int\frac{d\omega}{2\pi}\omega^{2n}\frac{C(k,\omega)}{\beta^{-1}\chi_0} = \int\frac{d\omega}{2\pi}\omega^{2n-2}\Sigma(k,\omega), \tag{4.16}$$

with $n \in \mathbb{N}^+$. The identities above are useful because the frequency moments of the spin correlation function can be expressed as the thermal expectation value, *within* the grand canonical ensemble, of the product of a $2n$-fold commutator with a spin operator

$$\mu_n = \frac{4}{k^2 L}\sum_{j,j'} e^{-ik(j-j')}\langle[...[\,[\hat{S}^z_j, H], H], ..., H]\hat{S}^z_{j'}\rangle, \tag{4.17}$$

where H is the Hamiltonian (1.27) and $\hat{S}^z_j$ corresponds to a spin within the bulk. In the limit of

infinite temperatures, these commutators can be evaluated exactly for given n.

4.2 Memory function Ansatz

We mainly focus on situations where no conserved quantities couple to the current, i.e. when $\Sigma(k,t)$ describes the regular component of the Kubo conductivity. We shall allow for non-analytic behavior of the memory function and assume that *a*t and close to the integrable limit $\Sigma(k,t)$ scales with time as $t^{-1-\alpha}$ in the hydrodynamic limit, and hence that any magnetization imbalance relaxes anomalously, i.e. as $\lim_{t\to\infty}\langle x^2\rangle \propto t^{1-\alpha}$. We relate the dynamical exponent (here α) to the microscopic parameters of our model by means of the set of exact sum rules (4.16).

The first three moments of the memory function can be shown to be in the long-wavelength limit

$$\mu_1 = \frac{1}{2}J_1^2 + 2J_2^2, \tag{4.18}$$

$$\mu_2 = \frac{1}{4}J_1^2\Delta^2 + J_2^2\Delta^2 - \frac{3}{2}J_1^2J_2\Delta + \frac{5}{2}J_1^2J_2^2, \tag{4.19}$$

$$\begin{aligned}\mu_3 = {} & \frac{1}{4}J_1^2\Delta^4 + J_2^2\Delta^4 + \frac{5}{16}J_1^4\Delta^2 + \frac{3}{2}J_2^4\Delta^2 + 10J_1^2J_2^2\Delta^2 \\ & -\frac{11}{4}J_1^2J_2\Delta^3 - \frac{5}{2}J_1^4J_2\Delta - \frac{27}{8}J_1^2J_2^3\Delta + \frac{7}{2}J_1^2J_2^4 \\ & +\frac{85}{16}J_1^4J_2^2,\end{aligned} \tag{4.20}$$

where the first moment yields nothing but the spin analog of the usual f-sum rule for the conductivity

$$\int_0^\infty d\omega\,\sigma(\omega) = \frac{\pi}{4}\left(\frac{1}{2}J_1^2 + 2J_2^2\right). \tag{4.21}$$

That all the moments of the memory function exists, which follows from eq. (4.17), means that both $\Sigma(k,\omega)$ and $C(k,\omega)$ have to fall off faster than any power-law for large frequencies. Although one can easily compute higher order moments, the reconstruction of the memory function from them is a well known ill-posed inverse problem. We shall instead adopt a three-parameter Gaussian memory Ansatz with the aforementioned low-frequency power-law behavior

$$\lim_{k\to 0}\Sigma(k,\omega) = C\,\frac{\omega_0^{-1-\alpha}}{\Gamma\left(\frac{1+\alpha}{2}\right)}\,|\omega|^\alpha \exp\left(-\left|\frac{\omega}{\omega_0}\right|^2\right), \tag{4.22}$$

where the parameters α and ω_0 are to be determined in terms of the moments eq. (4.18)–(4.20), $\Gamma(x)$ is the gamma function, and the amplitude C is fixed by the first sum rule to be $C = 2\pi\mu_1$.

We choose a Gaussian Ansatz for it leads to finite even moments of any order, and allows to

analytically solve the sum-rule equations for the two parameters determining it. Furthermore a direct approximation by Padé approximants to the short-time power series expansion (up to t^{14}) of the true memory function shows that at the shortest times it decays as a Gaussian, as can be clearly seen in the left panel of Fig. 4.1. Note this holds for both integrable and nonintegrable cases. Our Ansatz thus matches the known short-time behavior with the expected long-time behavior. The extent to which the Ansatz is an apt approximation for the true memory function can of course only be tested a posteriori.

Similar ideas have been used before in the context of high-temperature spin transport to obtain the diffusion constant of the integrable model [68–70]. Eq. (4.22) simply extends these ideas to allow for anomalous diffusion. Indeed for $\alpha = 0$ the Ansatz gives pure Gaussian decay, corresponding to diffusive modes i.e. $C(k,t) = \sum_j e^{ik.(r_j - r_0)} (S^z_j | S^z_0(t)) \sim e^{-D_s k^2 t}$, for the wavevector k and spin diffusion constant D_s. When $\alpha > 0$ this decay is further suppressed with a higher power of k and *subdiffusion* ensues, whereas when $\alpha < 0$ transport becomes *superdiffusive*.

We want to stress that, as it stands, eq. (4.22) assumes the spin current does not overlap with any of the local or quasilocal conserved quantities of the model, and hence it is only valid (i) for finite J_2 and $\Delta \in \mathbb{R}$; or (ii) in the integrable case ($J_2 = 0$) for $\Delta \geq 1$. Below we present a simple way of generalizing the sum-rule equations so that the Ansatz describes the regular component of the conductivity even when transport is ballistic.

Introducing eq. (4.22) into eq. (4.16) results in

$$\frac{\mu_n}{\mu_1} = \omega_0^{2n-2} \frac{\Gamma\left(\frac{2n-1+\alpha}{2}\right)}{\Gamma\left(\frac{1+\alpha}{2}\right)}. \tag{4.23}$$

where $n \in \mathbb{N}^+$. Solving the sum-rules equations yields an expression for the memory function which only depends on the microscopic parameters of the model Hamiltonian. Thus the dynamical exponent reads

$$\alpha(J_2, \Delta) = \frac{3\,\mu_2(J_2,\Delta)^2 - \mu_1(J_2)\mu_3(J_2,\Delta)}{\mu_1(J_2)\mu_3(J_2,\Delta) - \mu_2(J_2,\Delta)^2}, \tag{4.24}$$

and likewise

$$\omega_0(J_2,\Delta)^2 = \frac{2}{\alpha(J_2,\Delta)+1} \frac{\mu_2(J_2,\Delta)}{\mu_1(J_2)}, \tag{4.25}$$

where we have set J_1 as our energy scale.

4.3 Predictions

Let us employ the above formalism to study the integrable and nonintegrable cases separately — a lot more is known about the former to which comparison may be made [20, 25, 26, 29, 71].

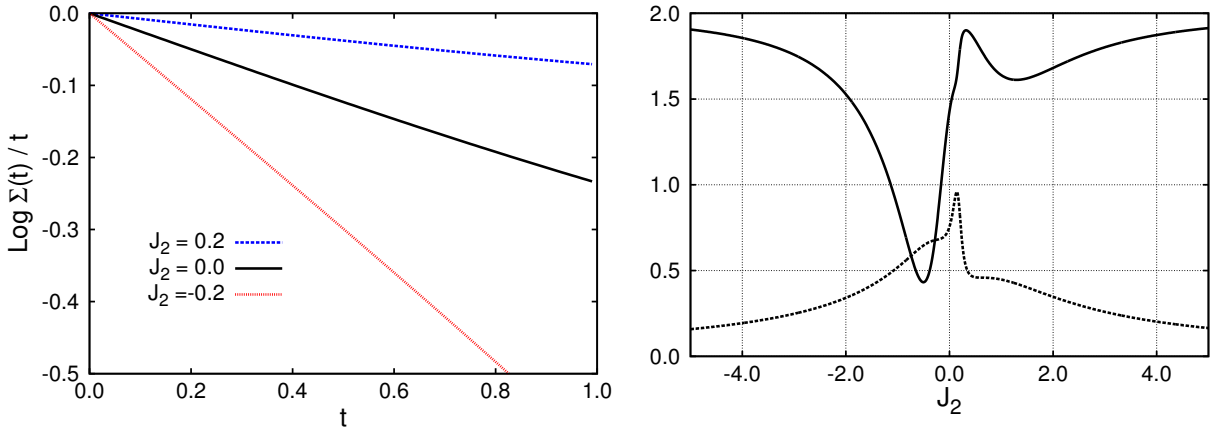

Figure 4.1: *L*eft: Padé approximant to the short-time power series expansion to $O[t^{14}]$ of the true memory function for three J_2 values and $\Delta = 1$. The data shows the memory function decays as a Gaussian at short times for the three J_2 values. *R*ight: memory function dynamical exponent (full line) "$1-\alpha$" characterizing the longitudinal spin damping $\lim_{t\to\infty}\langle(\Delta x)^2\rangle \sim t^{1-\alpha}$ for $\Delta = 1$ as a function of J_2. The range of J_2 values for which $\alpha > 0$ makes the system subdiffusive. The dashed line indicates the variation of ω_0^{-1} with J_2, also showing the asymmetry with respect to the sign of J_2.

4.3.1 Integrable case

As already discussed in section 1.2, in the integrable limit one needs to distinguish between three regimes with different transport properties, namely the gapless, isotropic and gapped phases of the XXZ model. Let us start with the gapless phase.

Gapless phase

It is rigorously known that in the gapless phase ($0 \leq \Delta < 1$) the Drude weight "D" is finite [60] and so the memory function Ansatz (4.22) should be modified accordingly to include a $4\beta^{-1}D\,\delta(\omega)$ contribution. This contribution only modifies the first sum rule and can be taken into account by explicitly subtracting it away from the first moment, i.e. $\mu_1 \to \mu_1 - (2/\pi)\beta^{-1}D$, so that the Ansatz still approximates the regular component of the Kubo conductivity.

Taking the Drude weight to be given by the Thermodynamic Bethe Ansatz result [61, 62]

$$\beta^{-1}D = 2\pi\frac{\gamma - \sin(2\gamma)/2}{16\gamma}, \tag{4.26}$$

with $\gamma = \cos^{-1}\Delta$, setting $J_2 = 0$ and using the modified the first moment in eq. (4.24) yields [72]

$$\alpha(0,\Delta) = -1 + \frac{16\Delta^2\cos^{-1}\Delta}{10\cos^{-1}\Delta + (5+4\Delta^2)\sin(2\cos^{-1}\Delta)}, \quad 0 \leq \Delta < 1. \tag{4.27}$$

This results implies the low-frequency spin conductivity displays *s*ubleading subballistic behavior of the form

$$\sigma'(\omega) \sim D\,\delta(\omega) + \omega^{\alpha}, \quad \text{with} \quad -1 < \alpha < -3/7. \tag{4.28}$$

In the section A below we investigate further the consequences of Eqs. (4.27) in the limit $\Delta \ll 1$, and find good agreement with numerical simulations.

Isotropic and gapped phases

Away from the gapless phase ($\Delta \geq 1$) the Drude weight vanishes. Setting $J_2 = 0$ in eq. (4.24) we get

$$\alpha(0, \Delta) = \frac{2\Delta^2 - 5}{2\Delta^2 + 5}. \tag{4.29}$$

Similarly, setting $J_2 = 0$ in eq. (4.25) we obtain

$$\omega_0(0, \Delta) = \frac{\sqrt{2\Delta^2 + 5}}{2}, \tag{4.30}$$

which implies increasing the anisotropy stretches the Gaussian and shortens the average collision time $\sim \omega_0^{-1}$. Let us now focus on the cases $\Delta = 1$ and $\Delta > 1$ separately, for the dynamical properties in these two regimes are known to be very different [19–21].

Isotropic point — at the isotropic point ($\Delta = 1$) eq. (4.29) predicts superdiffusive transport with the exponent $\alpha = -3/7$. Thus, within our approximation, any magnetic distortion scales with time as

$$\langle (\Delta x)^2 \rangle \sim t^{10/7} \approx t^{1.43} \tag{4.31}$$

in the long-time limit. Superdiffusion at the isotropic point has been predicted previously, both analytically with the scaling $\sim t^{12/7} \approx t^{1.71}$ in the continuum limit [73], and numerically, by means of the recursion method [74] ($\sim t^{1.26}$) and exact diagonalization [75] ($\sim t^{1.41}$). More recently t-DMRG studies [19–21] — both in unitary and nonunitary dynamics — also found superdiffusive transport with $\langle (\Delta x)^2 \rangle \sim t^{4/3} \approx t^{1.33}$. Our prediction is in good agreement with these numerical results and with the numeric simulations of section. 4.4.

Gapped phase — Eq. (4.29) gives a smooth interpolation between superdiffusive behavior at the isotropic point and no transport at the Ising limit (i.e. $\alpha \to 1$ as $\Delta \to \pm\infty$), thereby implying the possibility of anomalous diffusion for $\Delta > 1$, i.e. that increasing Δ continuously slows down the damping of the longitudinal component of an inhomogeneous magnetization from superdiffusive to subdiffusive spreading, making the system a perfect insulator (a system with a vanishing diffusion constant)for $\Delta > \sqrt{5/2}$ [72]. Interestingly enough, numerical simulations within the gapped regime show that (i) only the first two cumulants of the spin current operator scale diffusively whereas higher cumulants do not [63], which suggests the system is not truly normal diffusive in the presence of a gap; and that (ii) Gaussian relaxation (as opposite to exponential relaxation) dominates the long-time limit at the smallest nonzero wavevector of $C(k, t)$, which entails anomalous diffusion in finite chains [76]. However, there is disagreement on this, with normal diffusion being suggested for $\Delta > 1$, especially in the large Δ limit [19, 21, 77]. Given the good agreement found at the isotropic point between our approximation, the literature and the numerics of section 4.4, one could argue the Ansatz (4.22) may give a good description of AC transport within the gapped phase for anisotropies not too far from $\Delta = 1$. A

very different matter is the limit $\Delta \gg 1$, which our Ansatz does not capture. Let us therefore modify our Ansatz accordingly.

Large Δ limit — In the large Δ limit the eigenstates of the model are close to classical spin configurations. Consider spin flips between, say, second and third sites in a segment of an infinite chain. The four possibilities are: (i) ... $\downarrow\uparrow\downarrow\downarrow$ ..., (ii) ... $\uparrow\uparrow\downarrow\uparrow$ ..., (iii) ... $\uparrow\uparrow\downarrow\downarrow$ ..., (iv) ... $\uparrow\downarrow\uparrow\downarrow$ .... Spin flips from J_1 mix degenerate states (up to a splitting in J_1) in the first two cases, and states separated by $\pm\Delta$ in the last two cases — these are the only processes contributing to the conductivity. With these considerations in mind, the large-Δ memory function may be approximated by

$$\Sigma(\omega) = \frac{A}{2\sqrt{\pi\omega_A^2}}\left\{e^{-\left(\frac{\omega-\xi}{\omega_A}\right)^2} + e^{-\left(\frac{\omega+\xi}{\omega_A}\right)^2}\right\} + \frac{B}{\sqrt{\pi\omega_B^2}}\; e^{-\left(\frac{\omega}{\omega_B}\right)^2}. \tag{4.32}$$

This Ansatz involves five unknown parameters to be determined. Using the five known moments for the XXZ chain, the sum-rule eqs. (4.16) yield

$$\begin{aligned} A &= \frac{J_1^2}{4} - \frac{3J_1^4}{16\Delta^2}, \qquad \omega_A = J_1 \\ B &= \frac{J_1^2}{4} + \frac{3J_1^4}{16\Delta^2}, \qquad \omega_B = \sqrt{\frac{3}{2}}J_1, \\ \xi &= \Delta - \frac{J_1^2}{4\Delta}. \end{aligned} \tag{4.33}$$

With these results eq. (4.32) predicts the diffusion constant

$$\Sigma(\omega = 0) \approx \frac{J_1}{10}, \quad \text{for} \quad \Delta \gg 1. \tag{4.34}$$

The linear dependence of the diffusion constant with J_1 close to the Ising limit is consistent with earlier studies [19, 77]. Hence, eq. (4.32) is a much better Ansatz to be employed in the large-Δ limit, as opposed to Eq. (4.22). Let us note, nevertheless, that eq. (4.34) is in disagreement with Ref. [78] which suggests the diffusion constant saturates instead. In what follows we will not focus on the strongly interacting case but will limit to being close to the isotropic Heisenberg limit.

4.3.2 Nonintegrable case

We break integrability of the XXZ chain by including next-nearest neighbor spin flips with amplitude J_2. The full line in the right panel of Fig. 4.1 depicts the low-frequency dynamical exponent "$1-\alpha$" characterizing the longitudinal spin damping $\langle(\Delta x)^2\rangle \sim t^{1-\alpha}$, for $\Delta = 1$ as a function of J_2. This result shows the sign of the next-nearest neighbor spin-flip term has a strong effect on the spin dynamics: positive J_2 values enhance superdiffusion in a nonmonotonic way, whereas for some small range of negative J_2 values long-time transport is suppressed and

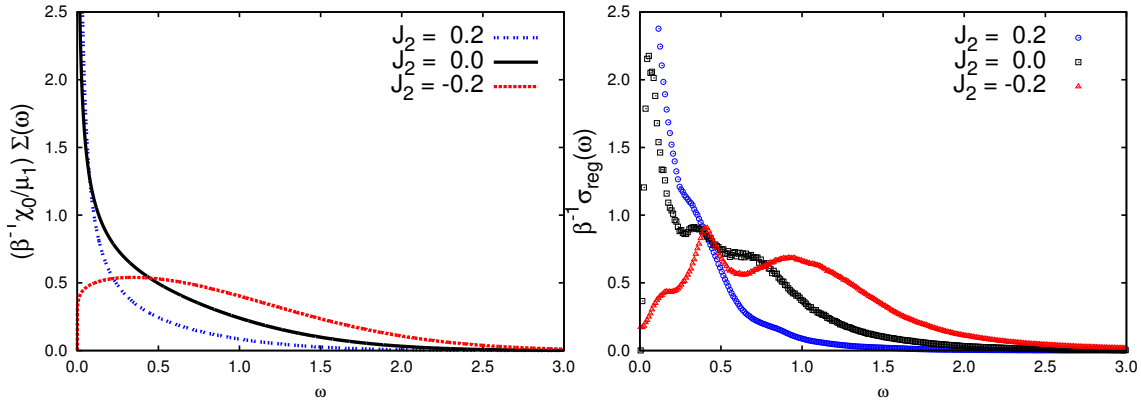

Figure 4.2: *L*eft: frequency dependence of the (normalized) memory function Ansatz, for $\Delta = 1$ and three values of J_2. Note the asymmetry for the transport rates with respect to the sign of J_2. *R*ight: normalized Kubo conductivity for a 20-site spin ring, computed within the canonical ensemble for states with zero total magnetization, and the same set of parameters as for the memory function (uniform binning, width = 0.01). All the given results are in units of J_1.

becomes subdiffusive. Transport suppression for small negative J_2 is remarkable, for one would expect that close to the integrable limit the "nearly-conserved" quantities dominate the long-time dynamics and slow down the decay of the current-current correlations. The dashed line in the right panel of Fig. 4.1 depicts the dependence of ω_0^{-1} on J_2, which is clearly consistent with the results for the dynamical exponent. We show in Fig. 4.2 the frequency dependence of our Ansatz for $\Delta = 1$ and three values of J_2 as compared to exact-diagonalization computations, the details of which can be found in section 4.4 below. Note again the sharp asymmetry of the transport rates with respect to the sign of J_2: positive J_2 shifts the spectral weight to lower frequencies and favors transport whereas negative J_2 shifts the spectral weight to higher frequencies, thereby implying slow collective modes. Both these aspects — the differences in low and high frequency response — are clearly present in the Kubo conductivity results, as can be seen in the right panel of Fig. 4.2, and may be confirmed by a simple calculation on a weakly perturbed 3-site chain, as we do below.

Microscopic mechanism — Our spin chain may be interpreted as a zig-zag ladder with J_2 acting along the rails and J_1 acting along the rungs. As discussed in chapter 2 positive J_2 values yield in-plane frustration in the ground state and, one may argue, tend to favor dimer spin configurations even at high temperatures. Such configurations effectively compete with the anisotropy, the dominant localizing mechanism, and lead to an enhancement of transport. Upon further increasing J_2 however, "frustration" becomes the main localizing mechanism and spin transport is slowed down until, for even larger J_2 values, the ladder starts decoupling into two "free" spin chains. We consider the limit $J_2 \gg 1$ more thoroughly in section A and find very good agreement between our Ansatz and the numerics.

We can corroborate the above picture for intermediate J_2 from a simple trimer calculation: consider a 3-site spin chain, with two up spins and one down spin. This system may be readily

shown to respond, through the current operator, eq. (1.32), only at two frequencies

$$\omega_{\pm} = \frac{1}{8}\left(\Delta - 6J_2 \pm \sqrt{(\Delta + 2J_2)^2 + 32}\right), \tag{4.35}$$

with the conductivity given by

$$\begin{aligned}\sigma(\omega) \;=\; & \frac{\omega_+^2\,\delta(\omega-\omega_+)}{32 + 4(2J_2+\Delta)^2 + 4(2J_2+V)\sqrt{(2J_2+\Delta)^2+32}} \\ & + \frac{\omega_-^2\,\delta(\omega-\omega_-)}{32 + 4(2J_2+\Delta)^2 - 4(2J_2+\Delta)\sqrt{(2J_2+\Delta)^2+32}},\end{aligned} \tag{4.36}$$

for small $J_2 \ll \Delta$ and $\omega_- < \omega_+$, with the latter difference increasing for $J_2 < 0$. Thus for positive J_2 the two frequency modes are constrained to be closer to each other, and with about the same spectral weight, whereas for negative J_2 the two modes separate out into a high- and a low-frequency mode, the latter being spectrally suppressed in amplitude. This means that in the presence of small negative next-nearest neighbor spin flips the system's dynamics gets slower due to the spectral redistribution. Such redistribution is predicted by our memory function Ansatz and is vindicated by the numerical linear response calculations, as shown in Fig. 4.2.

Note that setting $\Delta = 0$ in the above eq. (4.35) and (4.36) gives identical dynamical properties for both signs of J_2. This can also be seen directly in the first three moments, eq. (4.18)–(4.20): the odd powers of J_2 are always coupled to Δ. Hence, it is really the competition between frustration and interaction that begets the anomalous dynamics.

We finish this section with a comment and caveat: in what follows we will compare more thoroughly the picture emerging from our simple Ansatz, Eq. (4.22), with the spin conductivity of finite-size spin chains. We will find that intermediate and high frequency dynamics are indeed well modeled by our memory function in describing anomalous transport. Note however that in the long-time or low-frequency limit, the nonintegrable systems are all expected to be (normal) diffusive, with $\sigma(\omega \to 0) = \sigma_0$ (unless level repulsion sets in for the finite-L systems).

4.4 Numerics: Kubo conductivity

The infinite-temperature regular conductivity at frequency ω is computed from the Kubo formula

$$\lim_{\beta\to 0}\beta^{-1}\,\sigma_{\mathrm{reg}}(\omega) = \frac{\pi}{LZ}\sum_{m,n}|\langle\, m\,|\,\hat{j}\,|\,n\,\rangle|^2\,\delta(\omega - E_m + E_n), \tag{4.37}$$

which follows from eq. (1.25). The summation is over all the eigenstates of the model, the E_m's are the corresponding eigenvalues, Z is the partition function and $\hat{j}$ is the total spin current operator (1.32).

Before proceeding, a few comments on practical aspects are in order. Since $\hat{m}_z$ and $\hat{Z}$ commute with both $\hat{K}$ and $\hat{P}$, and that $[\hat{K},\hat{P}] = 0$ in the $k = 0$ sector and $[\hat{m}_z,\hat{Z}] = 0$ in the $m_z = 0$ sector, one can use this set of symmetries to block-diagonalise the Hamiltonian [57]. For finite J_2 and large L the energy-level statistics of each of these symmetry sectors are those of the Gaussian

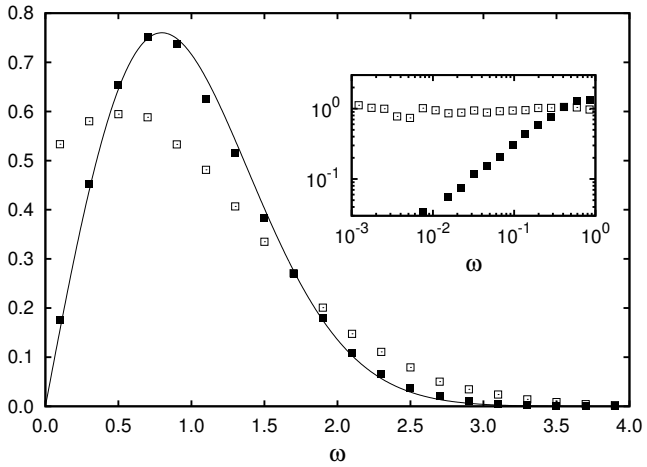

Figure 4.3: Filled squares: level-spacing distribution for a 20-site spin ring with $\Delta = 1$ and $J_2 = 0.2$ averaged over the different symmetry subsectors with zero total magnetization ($m_z = 0$). The inset shows the usual low-frequency linear decay of the level spacing distribution due to level repulsion. Empty squares: Level-spacing distribution for the states mixed by the spin current operator (1.32). Note the absence of level repulsion in this case which will be reflected in the conductivity. The ideal GOE distribution is shown as a full line in both plots.

orthogonal ensemble (GOE) [10]. However, as previously mentioned, the total spin current operator $\hat{j}$ is odd under both parity and spin-inversion and, consequently, its only nonvanishing matrix elements are those connecting symmetry subsectors with opposite (p, z). Thus, in the presence of spin-inversion symmetry and parity, the energy difference in the argument of the Dirac delta functions in the Kubo formula mixes different GOE spectra. The left of Fig. 4.3 illustrates the consequences of this: the filled squares show the level statistics taken within each symmetry sector and then averaged over; the correspondence with random matrix theory is evident. Empty squares, in contrast, correspond to the level spacing distribution for the set of states mixed by the current operator. The main aspect to be noted is the absence of level repulsion, which entails that for frequencies much smaller than the average level spacing, the conductivity, when computed in the canonical ensemble within the zero-magnetization sector, will not display the usual reduction due to the decrease of level pairs with such energy differences.

The right panel of Fig. 4.2 shows the Kubo conductivity for a 20-site spin chain with $\Delta = 1$ and three values of J_2 (in units of J_1). It is obtained by approximating the Dirac delta functions in Eq. (4.37) with uniformly spaced frequency bins, averaged over the different total momentum sectors of the symmetry block with vanishing total magnetization ($m_z = 0$). As pointed out above, the main feature of this result is the asymmetry with respect to the sign of J_2: in the presence of in-plane frustration the spectral weight is mainly located at low frequencies, whereas for negative J_2 the spectral weight is shifted to higher frequencies and shows a more complex structure, signaling slower collective excitations. We remark once again the qualitative agreement between this data set and the predictions from the memory function Ansatz (left panel of Fig. 4.2).

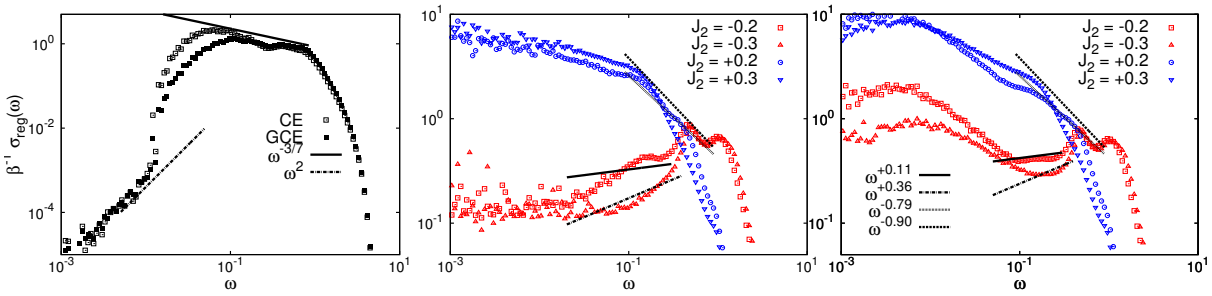

Figure 4.4: Mid-frequency power laws and ensemble dependence of the normalized high temperature conductivity. *L*eft: conductivity in canonical (CE) and grand canonical ensemble (GCE) of the $L = 18$ integrable chain. A superdiffusive power-law as obtained from the ansatz gives a good-fit before the low-frequency ω^2 behavior sets in; the latter is consistent with the argument in Ref. [79] at low-frequencies in the integrable chains. *C*enter: conductivity in nonintegrable $L = 18$ chains in the $m_z = 0$ sectors; the black lines correspond to power-law fits from the Ansatz, whose exponents are defined in the right panel of the figure. Note the behaviour predicted by the Ansatz is qualitatively and quantitatively consistent with the drift, and often values, of the power laws as $\pm J_2$ is changed. *R*ight: Same as middle panel but in the grand canonical ensemble. An extra peaking is observed at much lower-frequencies in all $J_2 \neq 0$ cases, which is a remnant of the finite-L Drude peak from the integrable limit (which is absent in the middle panel due spin-inversion symmetry).

To further study the long-time transport properties of our model, as well as the validity of the predictions from the previous sections let us consider Fig. 4.4. It shows the ensemble dependence of the conductivity, computed using logarithmically spaced frequency bins, together with the mid-frequency power-law predictions from the memory function Ansatz. Here we distinguish between canonical (CE) and grand canonical (GCE) ensemble calculations: in the former case we average over eigenstates with $m_z = 0$, whereas in the latter the average includes eigenstates from all the different magnetization sectors. Let us consider the integrable and nonintegrable case separately.

4.4.1 Integrable case

The left panel of Fig. 4.4 depicts the finite-size low-frequency conductivity for an 18-site isotropic Heisenberg chain. The first aspect ones notes is that at frequencies lower than $\omega \sim 0.1$ the conductivity abruptly drops, a feature which has been identify as a pseudogap in previous studies [80]. The difference between the two ensemble calculations at these frequencies has a simple explanation: at the isotropic point ($\Delta = 1$) the Drude weight *o*f small chains is finite and vanishes exponentially when increasing system size in the GCE, whereas it vanishes identically for any L due to spin-inversion in the CE. Hence we expect the regular part of the GCE conductivity to drop at higher frequencies – as compared with the CE calculation, in order to preserve the optical sum-rule, eq. (4.21). Since in the thermodynamic limit the Drude weight vanishes, such a difference between ensembles is nothing but a finite size effect. At even lower frequencies we observe the onset of a clear ω^2 power law. Such a ω^2 low-frequency behavior has been argued for in Ref. [79] for the integrable chain. However, by repeating our simulations for different chain lengths, we have observed the onset of the ω^2 behavior slowly moves towards

lower frequencies when increasing L (see Appendix B), thus indicating it corresponds to another finite-size effect. Hence, for the system sizes considered here we expect strong finite-size effects for frequencies $\omega \lesssim 0.1$.

Note that there is strong numerical evidence for superdiffusion at the isotropic point [19–21]. Remarkably, a superdiffusive power-law, as obtained from our Ansatz (4.22), fits well the data before the sudden drop of the conductivity.

4.4.2 Nonintegrable case

Consider first the center panel of Fig. 4.4, where we plotted CE data for four J_2 values. To begin with, note the strong suppression of spectral weight at low frequencies for negative J_2, and the absence of level repulsion at the lowest frequencies due to spin-inversion and parity symmetries (see Fig. 4.3). Most importantly, and focusing on frequencies $\omega \gtrsim 0.1$ (i.e. before the finite-size effects observed in the integrable limit set in) we see there is a frequency range on which the power laws obtained from our Ansatz, represented as black lines whose legend is shown in the right panel of the figure, are qualitatively consistent with the drift and power laws of the conductivity data for both frustrated and unfrustrated cases. Pivotally one can clearly identify from the exact-diagonalization data alone power-law behavior which signals anomalous diffusion processes occurring on a limited time domain.

These observations are interesting because even if anomalous transport shows up on a limited frequency range only, it might be enough to generate anomalous behavior in NMR experiments, as was argued by Sirker et al. for the gapless phase of the integrable model [81]: although normal diffusion was found to take place on a limited space-time domain, it was enough to give diffusive behavior to spin-lattice relaxation rates, in agreement with experimental findings in the 1D chain Sr_2CuO_3.

The right panel of Fig. 4.4 shows similar results for the conductivity computed in the GCE. For $\omega \gtrsim 0.1$ the qualitative agreement between the data and the Ansatz predictions persists. At frequencies $\omega \lesssim 0.1$ however, the conductivity displays an additional peak which can be understood as follows: for finite L the Drude weight in the integrable limit is finite; breaking integrability transfers the Drude peak's spectral weight to finite frequencies so that the optical sum-rule is satisfied [58]. Such a redistribution results in the low-frequency enhancement at $\omega \lesssim 0.1$, which then corresponds to a finite-size effect. We investigate further the role of finite-size effects by considering GCE data for different system sizes in section B.

In summary, we have seem the power laws obtained from the Ansatz (4.22) qualitatively describe the finite-frequency conductivity power laws observed in both canonical and grand canonical ensemble computation. These results entail the possibility of mid-frequency anomalous diffusion in nonintegrable systems.

CHAPTER 5

Conclusions

We have investigated quantum spin transport in clean spin 1/2 chains, at and away from integrability. Using exact diagonalization, a set of exact sum-rule moment relations and a memory function Ansatz we investigated the response of the XXZ model to next-nearest neighbor integrability-breaking spin flips both at zero and infinite temperatures. Depending on the sign of the perturbation the model displays in-plane frustration in its ground state which localizes the spin degrees of freedom.

At zero temperature we computed the spin stiffness (or superfluid density) using exact diagonalization and found an interaction-induced enhancement of the spin stiffness due to the competition between spin-dimer and Néel like configurations — the former favored by frustration, the latter by the spin anisotropy. Surprisingly a similar phenomenon was observed in this model at infinite temperatures.

In the high-temperature limit we analyzed two quantities: the spin stiffness and the regular component of the Kubo conductivity. If the former is finite the spin conductivity diverges and spin transport is thus ballistic. In nonintegrable systems this quantity usually vanishes (we have actually checked explicitly it vanishes for our model).

We investigated the influence of discrete symmetries (namely parity and spin-inversion) and ensemble (canonical or grand canonical) on the high temperature spin stiffness "D" in the XXZ model by exactly diagonalizing small spin chains. Introducing a flux provides a convenient way to break these symmetries and study their effect upon the numeric evaluation of D. We found that when spin-inversion symmetry is broken the dominant contributions to the spin stiffness come from nondegenerate states. In contrast, if spin-inversion is intact only degenerate states related to the Λ quantum loop symmetry contribute to D. Such Λ-degeneracies only appear for spin chains of length $L \geq 2N$, for anisotropies $\Delta = \cos(M\pi/N)$ with $N \in \mathbb{Z}^+$ and $M < N$ coprimes. These observations allowed us to identify the finite-size discrepancies between GCE computations for even- and odd-length chains reported in the literature as consequence of the absence/presence of spin-inversion symmetry in the model. We further found that within the gapless phase ($\Delta < 1$) and in the presence of a flux (i.e. when spin-inversion is broken and the Λ degeneracies are lifted) the finite-size spin stiffness extrapolates to either the recently computed lower-bounds or to the Thermodynamic Bethe Ansatz (TBA) solutions, independent of the ensemble used. In particular, convergence towards the TBA solution is found whenever

the previously reported low-frequency anomalies [51] are absent. In contrast, in the absence of a flux the large-current-carrying degenerate states related to the Λ symmetry only show up for system sizes $L \geq 2N$, where N can be large depending on the anisotropy. This symmetry thus plays an important role in contributing to the thermodynamic limit of D. In fact, we have checked that for GCE calculations excluding the $m_z = 0$ sector (i.e. no spin-inversion) convergence is still slow. Hence breaking spin-inversion is not enough — one also needs to break the Λ symmetry. Thus slow convergence towards the exact D-value should be expected for generically chosen Δ in the absence of a flux. Therefore if spin inversion is broken and the Λ-degeneracies lifted, say with a magnetic flux, in an even-length spin-1/2 XXZ chain then convergence of D to the thermodynamic limit is significantly improved.

Away from the gapless phase we confirm absence of ballistic transport for $\Delta \geq 1$, both in the grand canonical ensemble and the zero magnetization sector, with or without the discrete symmetries preserved. Finally, we remark that with increasing anisotropy the contribution to the spin stiffness from the zero magnetization sector goes from being the most dominant to the least dominant. Given that only this magnetization sector is affected by the $\hat{Z}$ symmetry, the role of this decreases with increasing the anisotropy in a grand canonical ensemble calculation.

We studied AC response in both integrable and nonintegrable limits of the model, analytically through a memory function Ansatz and numerically through exact diagonalization. At and close to the integrable limit we chose a memory function Ansatz that allowed for anomalous diffusion. We found in the XXZ model (i) superdiffusion at the isotropic point, with frequency dependent conductivity $\sigma'(\omega \to 0) \sim |\omega|^{-3/7}$ in close numerical agreement with recent t-DMRG computations; (ii) subleading subballistic behavior in the regular component of the conductivity within the gapless phase; and (iii) normal diffusion deep into the gapped phase, with a diffusion constant linearly proportional to the weak hopping.

We further find the sign of the integrability breaking perturbation matters: while positive spin-flips (in-plane frustration in the ground state) enhance spin transport, there is a narrow interval of negative spin-flips amplitudes for which transport is strongly suppressed. Transport suppression for small negative spin-flips amplitudes is remarkable, for one would expect that close to the integrable limit the "nearly-conserved" quantities dominate the long-time dynamics and slow down the decay of the current-current correlations. The resulting (anomalous) long-time transport tails as inferred from the regular conductivity of small spin chains (computed using exact diagonalization) are captured faithfully, qualitatively and quantitatively by the memory function Ansatz in all regimes: gapless, isotropic, and gapped for the integrable chain, as well as across vast parametric swathes of the nonintegrable chain. These results entail the possibility of mid-frequency anomalous diffusion in nonintegrable systems.

Bibliography

[1] N. Bloembergen, Physica **15** (1949) p. 386 (cit. on p. 2).

[2] L. Kadanoff and P. C. Martin, Ann. Phys. **24** (1963) p. 419 (cit. on p. 2).

[3] D. Forster, *Hydrodynamic fluctuations, broken symmetry and correlation functions*, W. A. Benjamin, Inc., 1975 (cit. on pp. 2, 6, 31, 32).

[4] B. Sutherland, *Beautiful models: 70 years of exactly solved quantum many-body problems*, World Scientific Publishing Co. Pte. Ltd, 2004 (cit. on p. 3).

[5] H. Bethe, Zeit. Phys. **71** (1931) p. 205 (cit. on p. 3).

[6] M. Lüscher, Nucl. Phys. B **117** (1976) p. 475 (cit. on p. 3).

[7] B. S. Shastry, Phys. Rev. Lett. **56** (1986) p. 1529 (cit. on p. 3).

[8] M. P. Grabowski and P. Mathieu, Ann. Phys. (N.Y.) **243** (1996) p. 299 (cit. on p. 3).

[9] X. Zotos, F. Naef, and P. Prelovsek, Phys. Rev. B **55** (17 1997) p. 11029 (cit. on pp. 3, 9, 10, 29).

[10] G. Montambaux et al., Phys. Rev. Lett. **70** (1993) p. 497 (cit. on pp. 3, 19, 40, 51).

[11] N. Motoyama, H. Eisaki, and S. Uchida, Phys. Rev. Lett. **76** (1996) p. 3212 (cit. on p. 3).

[12] A. V. Sologubenko et al., Phys. Rev. B **62** (2000) R6108 (cit. on p. 3).

[13] A. V. Sologubenko et al., Phys. Rev. B **64** (2001) p. 054412 (cit. on p. 3).

[14] M. Takigawa et al., Phys. Rev. Lett. **76** (1996) p. 4612 (cit. on p. 4).

[15] K. R. Thurber et al., Phys. Rev. Lett. **87** (2001) p. 247202 (cit. on p. 4).

[16] P. Jung and A. Rosch, Phys. Rev. B **76** (2007) p. 245108 (cit. on p. 4).

[17] P. Jung, R. W. Helmes, and A. Rosch, Phys. Rev. Lett. **96** (6 2006) p. 067202 (cit. on pp. 4, 5).

[18] V. K. Varma and R. J. Sánchez, Phys. Rev. A **92** (2015) p. 013618 (cit. on pp. 4, 11).

[19] M. Znidaric, Phys. Rev. Lett. **106** (2011) p. 220601 (cit. on pp. 5, 26, 36, 37, 42).

[20] M. Znidaric, A. Scardicchio, and V. K. Varma, Phys. Rev. Lett. **117** (2016) p. 040601 (cit. on pp. 5, 26, 34, 36, 42).

[21] M. Ljubotina, M. Znidaric, and T. Prosen, arXiv: 1702.04210 (2017) (cit. on pp. 5, 36, 42).

[22] R. Kubo, J. Phys. Soc. Jpn **12** (1957) p. 570 (cit. on pp. 7, 29).

[23] X. Zotos and P. Prelov šek, Phys. Rev. B **53** (3 1996) p. 983 (cit. on pp. 9, 10, 29).

[24] P. Mazur, Physica **43** (1969) p. 533 (cit. on p. 10).

[25] T. Prosen, Phys. Rev. Lett. **106** (2011) p. 217206 (cit. on pp. 10, 34).

[26] T. Prosen and E. Ilievski, Phys. Rev. Lett. **111** (2013) p. 057203 (cit. on pp. 10, 17, 23–27, 34).

[27] J. M. P. Carmelo, T. Prosen, and D. K. Campbell, Phys. Rev. B **92** (16 2015) p. 165133 (cit. on pp. 10, 21).

[28] J. M. P. Carmelo, T. Prosen, and D. K. Campbell, Nucl. Phys. B **914** (2017) p. 62 (cit. on p. 10).

[29] F. Heidrich-Meisner et al., Phys. Rev. B **68** (2003) p. 134436 (cit. on pp. 10, 17, 23, 26, 34).

[30] T. Mishra et al., Phys. Rev. B **87** (2013) p. 174504 (cit. on pp. 11, 15).

[31] T. Mishra, R. V. Pai, and S. Mukerjee, Phys. Rev. A **89** (2014) p. 013615 (cit. on pp. 11, 14).

[32] R. E. Peierls, Z. Phys **80** (1933) p. 763 (cit. on p. 12).

[33] F. Bloch, Phys. Rev. B **2** (1970) p. 109 (cit. on p. 12).

[34] Y. Imry, *Introduction to mesoscopic physics*, Mesoscopic Physics and Nanotechnology, Oxford: Oxford University Press, 2002 (cit. on p. 12).

[35] Y. Aharonov and D. Bohm, Phys. Rev. **115** (1959) p. 485 (cit. on p. 12).

[36] M. Büttiker, Y. Imry, and R. Landauer, Physics Letters **96A** (1983) p. 365 (cit. on p. 12).

[37] L. P. Lévy et al., Phys. Rev. Lett. **64** (1990) p. 2074 (cit. on p. 12).

[38] V. Chandrasekhar et al., Phys. Rev. Lett. **67** (1991) p. 3578 (cit. on p. 12).

[39] W. Kohn, Phys. Rev. **133** (1963) A171 (cit. on pp. 13, 15).

[40] B. S. Shastry and B. Sutherland, Phys. Rev. Lett. **65** (1990) p. 243 (cit. on pp. 13–15).

[41] G. Bouzerar, D. Poilblanc, and G. Montambaux, Phys. Rev. B **49** (1994) p. 8258 (cit. on pp. 13, 15).

[42] T. Giamarchi and B. S. Shastry, Phys. Rev. B **51** (1995) p. 10915 (cit. on p. 13).

[43] D. J. J. Scalapino, S. R. R. White, and S. Zhang, Phys. Rev. B **47** (1993) p. 7995 (cit. on p. 13).

[44] C. A. Hayward et al., Phys. Rev. Lett. **75** (1995) p. 926 (cit. on p. 13).

[45] L. N. Trefethen and D. I. Bau, *Numerical linear algebra*, Society for industrial and applied mathematics, 1997 (cit. on p. 14).

[46] P. Jordan and E. Wigner, Zeitschrift für Physik **47** (1928) p. 631 (cit. on p. 14).

[47] C. A. Stafford, A. J. Millis, and B. S. Shastry, Phys. Rev. B **43** (1991) p. 13660 (cit. on p. 15).

[48] T. Shirakawa and E. Jeckelmann, Phys. Rev. B **79** (2009) p. 195121 (cit. on p. 15).

[49] B. N. Narozhny, A. J. Millis, and N. Andrei, Phys. Rev. B **58** (1998) R2921 (cit. on p. 17).

[50] S. Mukerjee and B. S. Shastry, Phys. Rev. B **77** (24 2008) p. 245131 (cit. on pp. 17, 22).

[51] J. Herbrych, P. Prelovsek, and X. Zotos, Phys. Rev. B **84** (2011) p. 155125 (cit. on pp. 17, 25–27, 44).

[52] C. Karrasch et al., Phys. Rev. B **87** (24 2013) p. 245128 (cit. on p. 17).

[53] H. Castella, X. Zotos, and P. Prelov šek, Phys. Rev. Lett. **74** (6 1995) p. 972 (cit. on pp. 18, 29).

[54] T. Deguchi, K. Fabricius, and M. M., J. Stat. Phys. **102** (2001) p. 701 (cit. on pp. 18, 19, 21, 26).

[55] D. Braak and N. Andrei, Journal of Statistical Physics **105**.3 (2001) p. 677 (cit. on pp. 18, 26).

[56] K. Kudo and T. Deguchi, Phys. Rev. B **68** (5 2003) p. 052510 (cit. on p. 19).

[57] A. W. Sandvik, AIP Conf. Proc **1297** (2010) p. 135 (cit. on pp. 20, 39).

[58] M. Rigol and B. S. Shastry, Phys. Rev. B **77** (16 2008) p. 161101 (cit. on pp. 23, 42).

[59] E. Ilievski and J. D. Nardis, arXiv: 1702.02930 (2017) (cit. on pp. 23–25).

[60] T. Prosen, Phys. Rev. Lett. **106** (2011) p. 217206 (cit. on pp. 23, 35).

[61] X. Zotos, Phys. Rev. Lett. **82** (1999) p. 1764 (cit. on pp. 25, 35).

[62] J. Benz et al., J. Phys. Soc. Jpn. Supp. **74** (2005) p. 181 (cit. on pp. 25, 35).

[63] M. Znidaric, Phys. Rev. B **90** (2014) p. 115156 (cit. on pp. 26, 36).

[64] S. Mukerjee, V. Oganesyan, and D. A. Huse, Phys. Rev. B **73** (2006) p. 035113 (cit. on pp. 29, 32).

[65] R. Zwanzig, *Statistical mechanics of irreversibility*. Ed. by W. E. Britten, B. Downs, and J. Downs, vol. 3, Lectures in theoretical physics (Boulder), Interscience, 1961 (cit. on p. 30).

[66] H. Mori, Prog. Theo. Phys. **34** (1965) p. 423 (cit. on p. 30).

[67] B. J. Berne and G. D. Harp, Adv. Chem. Phys. **XVII** (1970) p. 63 (cit. on p. 30).

[68] H. Mori and K. Kawasaki, Prog. Theo. Phys. **27** (1962) p. 529 (cit. on pp. 31, 34).

[69] P. G. De Gennes, J. Phys. Chem. Solids **4** (1958) p. 223 (cit. on p. 34).

[70] H. S. Bennett and P. C. Martin, Phys. Rev. **138** (1965) A608 (cit. on p. 34).

[71] R. J. Sánchez and V. K. Varma, arXiv: 1704.04273 (2017) (cit. on p. 34).

[72] We point that this smoothly varying exponent might be an artefact of our 3-parameter ansatz. An obvious way to improve upon this is to introduce more sophisticated Ansätze that require higher moments; so far our extended choices failed to provide a consistent hydrodynamic picture for the different systems we studied, i.e. systems with integrable and nonintegrable limits. We believe finding a judicious choice that captures the ballistic-superdiffusive-diffusive sharp jumps across the isotropic point, as numerics seems to suggest (although still only arguably) will not be easy, which we leave for future work. (cit. on pp. 35, 36).

[73] M. Chertkov and I. Kolokolov, Phys. Rev. B **49** (5 1994) p. 3592 (cit. on p. 36).

[74] M. Böhm et al., Phys. Rev. B **49** (22 1994) p. 15669 (cit. on p. 36).

[75] K. Fabricius and B. M. McCoy, Phys. Rev. B **57** (14 1998) p. 8340 (cit. on p. 36).

[76] R. Steinigeweg et al., Phys. Rev. B **85** (21 2012) p. 214409 (cit. on p. 36).

[77] R. Steinigeweg and R. Schnalle, Phys. Rev. E **82** (2010) p. 040103 (cit. on pp. 36, 37).

[78] C. Karrasch, J. E. JMoore, and F. Heidrich-Meisner, Phys. Rev. B **89** (2014) p. 075139 (cit. on p. 37).

[79] J. Herbrych, R. Steinigeweg, and P. Prelov šek, Phys. Rev. B **86** (11 2012) p. 115106 (cit. on p. 41).

[80] P. Prelov šek et al., Phys. Rev. B **70** (2004) p. 205129 (cit. on p. 41).

[81] J. Sirker, R. G. Pereira, and I. Affleck, Phys. Rev. B **83** (3 2011) p. 035115 (cit. on p. 42).

APPENDIX A

Approaching the free-particle limit

The model Hamiltonian Eq. (1.27) becomes a free model when either the anisotropy Δ is set to zero in the integrable limit, or for large $J_2 \to \infty$. In this section we consider the transport properties of the model as one approaches these two limits.

A.1 Small Δ limit of the integrable chain

We have shown in Sec. 4.2 the Ansatz defined in Eq. (4.22) predicts the low-frequency subleading behavior $\sigma'(\omega) \sim D\,\delta(\omega) + \omega^{\alpha}$ for the spin conductivity within the gapless phase, with the dynamical exponent lying in the interval $-1 < \alpha < -3/7$. More precisely, the *r*egular component of the conductivity shows subballistic behavior, smoothly going towards ballistic transport as Δ goes to zero

$$\Sigma(\omega) \approx \frac{2\pi}{5} \frac{\Delta^2}{\omega^{1-\frac{4\Delta^2}{5}}} e^{-\frac{4}{5}\omega^2} + O\left(\Delta^4\right), \quad \text{for} \quad \Delta \ll 1. \tag{A.1}$$

This regular component vanishes exactly at $\Delta = 0$, with a subleading behaviour approximated by $\omega^{-1+4\Delta^2/5} \approx \omega^{-1}$. Hence the conductivity in the XX chain is given by a $\delta(\omega)$ contribution as expected. Note that the small-Δ power-law behavior *does not* extend to the lowest frequencies and so the moments are still well defined.

In the left panel of Fig. A.1 we contrast the Kubo conductivity between the isotropic point and the small-Δ limit. Two points are noteworthy: (i) there are clear differences between the power laws about $\omega \approx 0.1$ for the two cases, with $\sigma(\omega) \sim \omega^{-1}$ being approximately satisfied for the small Δ chain; (ii) also for $\Delta = 0.05$ there is a Δ^2 drop between the end of the ω^{-1} power-law and the onset of the ω^2 finite-size-effect power-law that was discussed in the previous appendix; this is in contrast to the isotropic point where the drop to the ω^2 power law is immediate. Such Δ^2 drop is in line with the Ansatz prediction Eq. (A.1).

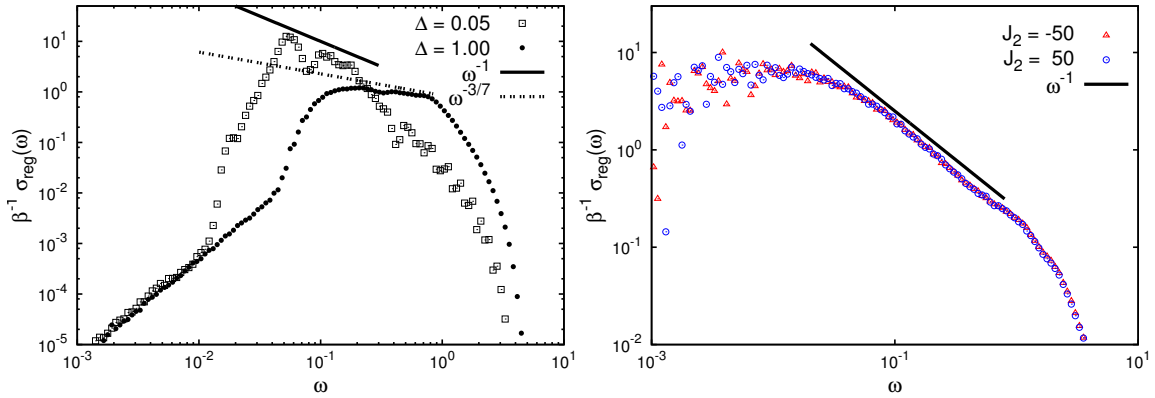

Figure A.1: $L = 18$ Kubo conductivity of fluxed chains in the grand canonical ensemble for extreme limits of Hamiltonian parameters. *Left panel*: the integrable chain comparing the small Δ limit with the isotropic point, the former fitting a steeper power-law ($\approx \omega^{-1}$) at mid-frequencies as predicted by the Ansatz Eq. (A.1) before a Δ^2 drop (which occurs well before the onset of ω^2 finite-size effect as in the isotropic point) sets in, which is also in line with the Ansatz prediction (A.1). *Right panel*: the nonintegrable chain for large J_2 limit where the Ansatz predicts an insensitivity to the sign of J_2. This latter prediction and the associated power-law $\approx \omega^{-1}$ given by Eq. (A.2) is vindicated by the displayed numerics at mid-frequencies.

A.2 Large J_2 limit

For large J_2 the spin chains decouple into two independent chains. Moreover, from the results shown in the right panel of Fig. 4.1, we expect the $\pm J_2$ dynamical responses to be identical as $J_2 \to \infty$, with $\alpha \to -1$, as in the small Δ limit treated in the preceding paragraphs. Note that for $1 \ll J_2 \neq \infty$ the system is still nonintegrable and therefore normal diffusion is expected at long times. In this limit, for $\omega \ll \omega_0(J_2 \to \infty, 1) = \sqrt{5}/2$, our Ansatz predicts

$$\Sigma(\omega) \approx \frac{49\pi}{10} \frac{1}{\omega^{1-\frac{49}{20J_2^2}}} + O\left(\frac{1}{J_2}\right), \quad \text{for} \quad |J_2| \gg 1, \tag{A.2}$$

which shows the symmetry with respect to sign of J_2 is restored. This restoration of the symmetry and the actual power-law at mid-frequencies being close to -1 is supported by the numerics as displayed in the right panel of Fig. A.1.

APPENDIX B

Finite-size effects in the low-frequency conductivity

To study how finite-size effects enter our exact diagonalization calculations, we repeated our GCE simulations for spin rings of different system sizes, pierced with an irrational magnetic flux. Fig. B.1 shows our results for $\Delta = 1$ and $J_2 = 0.0$ (left), 0.2 (center) and -0.2 (right), in units of J_1. The flux breaks spin-inversion, parity and time-reversal symmetry (here labeled as $\hat{K}$) but preserves the symmetry under the combined operation $(\hat{K} \times \hat{P})$. As discussed in chapter 3 breaking these symmetries generically accelerates convergence to the thermodynamic limit.

Now, all our *finite-size spin chains have a finite Drude weight (even for finite J_2) in the symmetry sectors of finite m_z. Breaking spin-inversion with the magnetic flux yields a finite Drude weight within the sector of zero total magnetization as well, thereby enhancing the GCE value of the Drude weight — again, as discussed in chapter 3. Thus in fluxed integrable chains we expect the regular conductivity to drop at higher frequencies as compared to unfluxxed chains, for the optical sum rule to hold. Comparing the left panels of Fig. 4.4 and Fig. B.1 shows this is indeed the case. Most importantly, note from Fig. B.1 the ω^2 behavior shows up for $\omega \lesssim 0.1$ and moves slowly to lower frequencies when increasing system size, which identifies it as a finite-size effect.

Let us now discuss the results for the nonintegrable chains. Firstly, we point out that the invariance under $(\hat{K} \times \hat{P})$ implies the energy pairs entering the Kubo formula for nonintegrable chains belong to a single GOE [10] and, consequently, that the conductivity for finite J_2 will show level repulsion at frequencies small compared with the average level spacing. One can clearly identify the onset of level repulsion in the center and right panels of Fig. B.1 as the linear drop of the conductivity at the lowest frequencies, marked with dashed lines. A bit more tricky is the increase with system size of the low-frequency enhancement before the onset of level repulsion. We identify two competing effects: first, and as pointed out above, breaking integrability transfers the Drude peak's spectral weight *from the integrable limit to finite frequencies; the strength of this effect should decrease when increasing system size. Second, the finite Drude weight of the nonintegrable chain itself rapidly decreases with system size, the corresponding spectral weight being shifted to finite frequencies. The combination of these two effects yields the low-frequency enhancement of the conductivity for $\omega \lesssim 0.1$, which

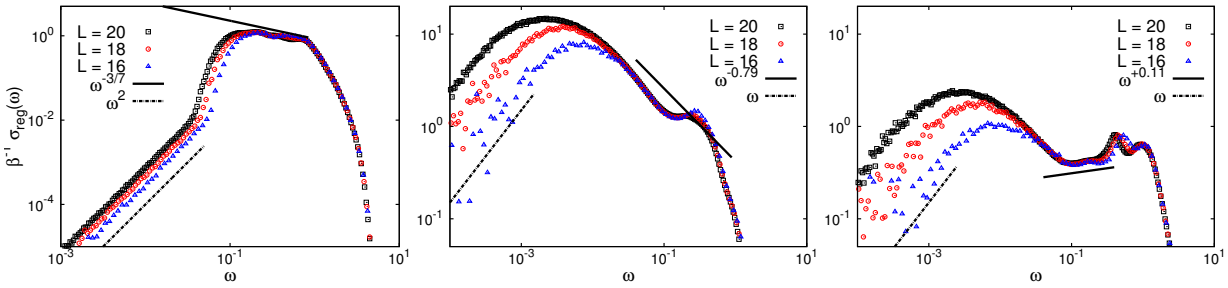

Figure B.1: low-frequency Kubo conductivity for spin rings of different length, pierced by an irrational magnetic flux and *a*veraged over all magnetization sectors. The parameters are $\Delta = 1$ and $J_2 = 0.0$ (left), 0.2 (center) and -0.2 (right). The black full lines in the plots correspond to the power laws obtained with the sum-rule method, Eq. (4.24), whereas the dotted lines are proportional to either ω^2 or ω. The latter case signals the onset of level repulsion.

then corresponds to a finite-size effect.

List of Figures

List of Tables